AFRL-RX-WP-TP-2012-0399

STRENGTHENING AND PLASTIC FLOW OF Ni3Al ALLOY MICROCRYSTALS (PREPRINT)

D.M. Dimiduk, M.D. Uchic, P.A. Shade, and C. Woodward
Metals Branch
Structural Materials Division

S.I. Rao and G.B. Viswanathan
UES, Inc.

E. Nadgorny
Michigan Technological University

S. Polasik, D. Norfleet, and M. Mills
The Ohio State University

AUGUST 2012
Interim

Approved for public release; distribution unlimited.

See additional restrictions described on inside pages

STINFO COPY

AIR FORCE RESEARCH LABORATORY
MATERIALS AND MANUFACTURING DIRECTORATE
WRIGHT-PATTERSON AIR FORCE BASE, OH 45433-7750
AIR FORCE MATERIEL COMMAND
UNITED STATES AIR FORCE

REPORT DOCUMENTATION PAGE

Form Approved
OMB No. 0704-0188

The public reporting burden for this collection of information is estimated to average 1 hour per response, including the time for reviewing instructions, searching existing data sources, searching existing data sources, gathering and maintaining the data needed, and completing and reviewing the collection of information. Send comments regarding this burden estimate or any other aspect of this collection of information, including suggestions for reducing this burden, to Department of Defense, Washington Headquarters Services, Directorate for Information Operations and Reports (0704-0188), 1215 Jefferson Davis Highway, Suite 1204, Arlington, VA 22202-4302. Respondents should be aware that notwithstanding any other provision of law, no person shall be subject to any penalty for failing to comply with a collection of information if it does not display a currently valid OMB control number. **PLEASE DO NOT RETURN YOUR FORM TO THE ABOVE ADDRESS**.

1. REPORT DATE ***(DD-MM-YY)*** August 2012	**2. REPORT TYPE** Technical Paper	**3. DATES COVERED *(From - To)*** 1 July 2012 – 1 August 2012

4. TITLE AND SUBTITLE
STRENGTHENING AND PLASTIC FLOW OF Ni3Al ALLOY MICROCRYSTALS (PREPRINT)

5a. CONTRACT NUMBER
In-house

5b. GRANT NUMBER

5c. PROGRAM ELEMENT NUMBER
62102F

6. AUTHOR(S)
D.M. Dimiduk, M.D. Uchic, P.A. Shade, and C. Woodward (AFRL-RXCM)
S.I. Rao and G.B. Viswanathan (UES, Inc.)
E. Nadgorny (Michigan Technological University)
S. Polasik, D. Norfleet, and M. Mills (The Ohio State University)

5d. PROJECT NUMBER
4347

5e. TASK NUMBER
20

5f. WORK UNIT NUMBER
X071

7. PERFORMING ORGANIZATION NAME(S) AND ADDRESS(ES)
Metals Branch (AFRL/RXCM)
Structural Materials Division
Air Force Research Laboratory, Materials and Manufacturing Directorate
Wright-Patterson Air Force Base, OH 45433-7750
Air Force Materiel Command, United States Air Force

8. PERFORMING ORGANIZATION REPORT NUMBER
AFRL-RX-WP-TP-2012-0399

9. SPONSORING/MONITORING AGENCY NAME(S) AND ADDRESS(ES)
Air Force Research Laboratory
Materials and Manufacturing Directorate
Wright-Patterson Air Force Base, OH 45433-7750
Air Force Materiel Command
United States Air Force

10. SPONSORING/MONITORING AGENCY ACRONYM(S)
AFRL/RXCM

11. SPONSORING/MONITORING AGENCY REPORT NUMBER(S)
AFRL-RX-WP-TP-2012-0399

12. DISTRIBUTION/AVAILABILITY STATEMENT
Approved for public release; distribution unlimited. Preprint to be submitted to Philosophical Magazine.

13. SUPPLEMENTARY NOTES
The U.S. Government is joint author of this work and has the right to use, modify, reproduce, release, perform, display, or disclose the work. PA Case Number and clearance date: 88ABW-2012-2092, 5 April 2012. This document contains color.

14. ABSTRACT
Ni3Al alloys exhibit unique deformation characteristics at small scales that are tied to their unique dislocation core structures. The present work examines microcrystal strengthening and flow for a binary Ni3Al alloy and two alloys containing -0.25 % Hf and -1.0 % Ta, and evaluates their response relative to known dislocation mechanisms for this material and sample size effects in other materials. The work includes analysis of the flow-stress anomaly mechanisms, dislocation velocity, the single-arm source model, exhaustion strengthening and dislocation multiplication for describing the response of Ni3Al alloy microcrystals. While aspects of the flow-stress anomaly mechanisms and a form of the single-arm source model work remarkably well to describe the response, other limitations exist for understanding Ni3Al behavior from current data and models. A primary need is to understand the nature of double cross slip and dislocation sources that trigger the onset of flow and limit size-dependent strengthening.

15. SUBJECT TERMS
strengthening mechanisms, deformation mechanisms, size effects, microcrystals, dislocations, tem (transmission electron microscopy), plasticity

16. SECURITY CLASSIFICATION OF:			**17. LIMITATION OF ABSTRACT:**	**NUMBER OF PAGES**	**19a. NAME OF RESPONSIBLE PERSON** (Monitor)
a. REPORT Unclassified	**b. ABSTRACT** Unclassified	**c. THIS PAGE** Unclassified	SAR	48	Andrew Rosenberger **19b. TELEPHONE NUMBER** *(Include Area Code)* N/A

Strengthening and plastic flow of Ni_3Al alloy microcrystals

D.M. Dimiduk, M.D. Uchic, S.I. Rao[+], P.A. Shade, C. Woodward, G.B. Viswanathan,[+]
E. Nadgorny,* S. Polasik,^[1] D. Norfleet^[2] and M. Mills^

Air Force Research Laboratory, Materials and Manufacturing Directorate, AFRL/RXLM
Bldg 655, 2230 10th St, Wright-Patterson AFB, OH 45433-7817, USA

[+]*UES, Inc, 4401 Dayton-Xenia Rd., Dayton, OH 45432, USA*

**Physics Department, Michigan Technological University, Houghton, MI 49931, USA*

^*Department of Materials Science and Engineering, The Ohio State University,*
2041 College Rd, Columbus, OH 43210

ABSTRACT

Ni_3Al alloys exhibit unique deformation characteristics at small scales that are tied to their unique dislocation core structures. The present work examines microcrystal strengthening and flow for a binary Ni_3Al alloy and two alloys containing -0.25 % Hf and -1.0 % Ta, and evaluates their response relative to known dislocation mechanisms for this material and sample size effects in other materials. The work includes analysis of the flow-stress anomaly mechanisms, dislocation velocity, the single-arm source model, exhaustion strengthening and dislocation multiplication for describing the response of Ni_3Al alloy microcrystals. While aspects of the flow-stress anomaly mechanisms and a form of the single-arm source model work remarkably well to describe the response, other limitations exist for understanding Ni_3Al behavior from current data and models. A primary need is to understand the nature of double cross slip and dislocation sources that trigger the onset of flow and limit size-dependent strengthening.

---

[1] Current address: S. Polasik
[2] Current address: D. Norfleet

INTRODUCTION & BACKGROUND

A remarkable aspect of microcrystal deformation, at sizes greater than ~1 μm, is the characteristics of the stress-strain curves that are qualitatively independent of material type. For example, FCC and BCC metals, as well as LiF in both irradiated (point defect laden) and pure form, exhibit the following attributes: i) size-dependent microstrain stresses as the sample size is reduced, ii) sample-size dependent flow stresses once dislocations multiply, iii) small plastic strain bursts together with severe size-dependent hardening over a finite strain range (sometimes several percent strain), iv) stochastic variations in the flow stress at a given sample size, v) intermittency or plasticity avalanches during flow and, vi) size-dependent strengths and avalanche properties that depend upon the dislocation density of the material [1]. These features manifest themselves even though dislocation properties differ across these materials.

Both simulations and experiments suggests that microcrystals smaller than ~1 μm have few dislocations and some of these may be eliminated under load, resulting in strengthening by "dislocation starvation," much like the findings for metal crystals in the form of whiskers [2, 3]. Evidence suggests this effect diminishes for larger microcrystals when compared to other mechanisms. Selected studies show that an excess dislocation density may form during microcrystal deformation, particularly when using a testing apparatus that constrains lateral motion of the loading platen and/or for samples having a low height-to-diameter ratio [41]. However, there is no current analysis that ties the attributes of microcrystal behavior to the formation of an excess dislocation density; thus, explanations must arise elsewhere, both from theory and simulations [1, 4, 5].

Currently, the microcrystal findings are self-consistently explained via two dominant dislocation micromechanisms. First, dislocation sources are on average shortened by the restricted sample size as dislocations intersect free surfaces—the 'source truncation' effect [3, 5-10]. Strengthening ensues from this mechanism even at the proportional limit through to small strains. The second mechanism was introduced by Gil Sevillano, et. al., through analysis of dislocation ensemble characteristics, before the first microcrystal experiments [11, 12]. The mechanism is called 'exhaustion hardening' or more generally 'mean-field breakdown.' The essential ideas stem from considering sample-size effects for dislocation percolation through a point-obstacle field, as pertinent to forest dislocation strain hardening. These investigators showed that as long as sample dimensions exceed the correlation length for the forest at a particular dislocation density (ρ_{total}), the strain-hardening rate (SHR) is sample-size independent. However, at smaller sizes, the distribution of segment lengths is truncated, thereby eliminating available sources at a given stress and strengthening ensues while the SHR diminishes. The mean-field limit for forest hardening cannot yet be quantitatively analyzed using 3-dimensional dislocation simulations since computers cannot yet attain the necessary simulation cell size, dislocation densities or appropriate dislocation interactions and multiplication for the ensemble [5, 13]. Nonetheless simulations qualitatively show the effect in conjunction with source-truncation via localized dislocation interactions [3, 5, 14]. Importantly, both mechanisms illustrate the importance of 'weakest links' of the dislocation ensemble for controlling flow stress in both micro- and macro-scale crystals.

The Ni_3Al alloys are unusual because formation, motion and 'locking' of screw-character dislocations, most notably from room temperature to ~600°C, results in anomalous strengthening with temperature. Superlattice dislocations (superdislocations) having extended core structures show thermally-activated changes to the mobility of screw-character components. These dislocations progressively transform via cross slip from a planar glissile core on the octahedral {111} glide planes, to one that is non-planar and partially spread on both the octahedral plane and the {010} cubic plane [15, 16]. This leads to anisotropic and faceted glide loops consisting of straight screw-character segments or Kear-Wilsdorf locks (KWL) joined by segments of the remaining characters as macro kinks (MK) [17-19]. Throughout the 1980's and mid 90's research examined the processes of KWL formation and their relationship to the flow stress anomaly. TEM analysis showed that the configurations partially separate in the cubic plane (incomplete KWL) or, fully extend in the cubic plane at the equilibrium separation distance for the superlattice partial dislocations (complete KWL) [20-23]. Building on these ideas, later work sought to i) reconcile the models for the dislocation behavior with physical observations of dislocations structures and deformation responses, ii) advance the micro-mechanistic observations within quantitative analytical models, iii) study the dislocation processes through computer simulations and, iv) to develop constitutive models of the behavior [24-34].

All of the studies point to the critical role of dislocation locking and exhaustion via KWL formation as a controlling mechanism, which in turn depends on the temperature-dependent distribution of mobile MK and KWL defeat. However, the studies do not sufficiently treat dislocation multiplication as an important companion to exhaustion when flow extends beyond microstrains. Having formed such MK and KWL configurations, glide must proceed via lateral motion of MKs and/or stress-assisted unlocking of KWL configurations—processes that remain in detailed dispute even to the present time. These unique dislocation attributes lead to distinct flow attributes including the positive temperature dependence of the flow stress and SHR, an offset-strain dependence of these quantities, unusually high SHR in the microstrain regime, orientation-dependent tension-compression (T-C) asymmetry, partially-to-fully reversible flow behavior during successive two-step (T_1 and T_2) deformation sequences and, a relatively low strain-rate sensitivity and its temperature dependence [33, 34].

Against this background of microcrystal and Ni_3Al alloy behavior, the present study examines Ni_3Al alloys in the form of microcrystals. Importantly, like certain other materials whose mechanical behavior has been evaluated in microcrystal form, nearly all aspects of the dislocation behavior are well studied for macroscopic Ni_3Al alloy crystals, forming a foundation for interpreting the testing results. The present studies may also provide insights into unresolved aspects of understanding the macro scale flow stress anomaly.

MATERIALS & EXPERIMENTS

Three Ni_3Al alloys were selected for the present work. The binary material is a baseline, while alloys with 0.25 % Hf and 1.0 % Ta additions progressively raise both the antiphase boundary (APB) and complex stacking fault (CSF) energies [29, 35]. Table I shows the alloy compositions in atomic percent, together with key alloy parameters including the systematic changes to {111} and {001} plane APB energies and, the complex stacking fault energies (Γ_{111}, Γ_{001} and Γ_{csf}, respectively) with composition and a reference for those values. The alloys were prepared as single crystal batches for prior studies of the bulk Ni_3Al crystal behavior reported within prior literature [36-38]. For this study, following annealing the -0.25 % Hf alloy was examined using TEM methods and was found to contain a nominal dislocation density of 5.2 x 10^{11}/m^2 [39].

The methods of the microcompression technique are described in several publications [40-42]. Isolated single-crystal columns were formed in relief within a prepared single crystal surface using either an FEI Strata DB235 or Nova Nanolab FIB-SEM. The surface normal of the prepared bulk crystal is the axial orientation of the columnar single crystal specimens, in this case <123>. Multiple crystals were prepared at each of the selected diameters (0.5 – 43 μm) for each alloy and, SEM images were used to measure the sample dimensions prior to testing. The crystals were tested at room temperature using a nanoindentation system (MTS Nanoinstruments Nano XP, and Nano II) using a diamond flat punch tip. A nominal strain rate of 1 x 10^{-4}/s and a data acquisition rate of 5 Hz were used for a majority of the tests while a sampling frequency of 500 Hz was used for selected tests. Processing and analysis of the testing data followed previously described procedures [12, 41, 43].

To compare the variations of flow stress among alloys, given the wide statistical scatter among stress-strain curves, a technique was devised to compute average stress-strain curves for sets of crystals at each sample size. First, the stress-strain curves were shifted on the strain scale relative to each other by selecting one of the curves as a reference and aligning the others to it at a selected stress level in the loading regime. The loading reference stress was chosen at a 5 – 15 MPa lower value than that required to operate a single-arm dislocation source, estimated for each sample size using the model introduced by Parthasarathy, et. al., scaled for Ni_3Al parameters [6]. The selection assumes that on average, microcrystal strengthening processes prevent flow for stresses lower than the single-arm source stress. Once the stress-stain curves were shifted, the recorded stress data for each crystal was sorted into uniformly spaced strain bins. Stresses were averaged within each bin to determine the average stress as a function of strain. Using the Schmid factor, the average engineering-stress versus engineering-strain data were converted to average shear stresses and approximate shear strains. No geometric corrections were used for determining shear strains, thus significant errors exist for large strain values; however, these values are not used for subsequent analyses.

Following deformation testing, selected crystals were examined in the TEM to evaluate the dislocation structures associated with deformation. Samples were prepared using foils sectioned parallel to both the loading axis and the primary octahedral slip plane, using previously described specimen preparation techniques [39, 44].

RESULTS

Stress-Strain Behavior

Figure 1a shows the binary Ni_3Al engineering stress–strain curves for <123> oriented microcrystals of the present study. As mentioned previously for other microcrystals, the Ni_3Al alloys exhibit: i) increasing micro stresses as the sample size is reduced, ii) sample-size dependent flow stresses and exhaustion hardening, iii) small plastic strain bursts during the finite exhaustion hardening strain range, iv) stochastic variations in the specific-sample flow stress and, v) selectively, intermittency or plasticity avalanches during flow for nominally continuous loading. Variations with initial dislocation density were not examined. While all samples exhibit plasticity avalanches, one may recognize that the nature of the plasticity bursts changes as the sample size decreases. For samples below ~10 μm, the flow curves tend to exhibit a sharp transition from loading to breakaway flow; much sharper than the stair-step like flow of the larger binary Ni_3Al samples. This feature—rapid breakaway shear glide to large strains (sometimes approaching ~50 % that is initiated at less than 1 % loading strain) is more pronounced for the Ni_3Al alloys than for other materials. In addition, for the largest microcrystals the nominal SHR are several times greater than for macroscopic crystals (Fig. 1a). The measured SHR in shear for these microcrystals in Stage I is ~K_s/260, where K_s is the anisotropic shear modulus, while the macroscopic binary Ni_3Al crystals exhibit a Stage I SHR that is a factor ~3 lower, while FCC metals in Stage I are ~3x lower still.

A comparison of the set-average shear stress versus nominal shear-strain curves for selected crystal sizes of each alloy are shown in Fig. 1b. The comparisons show that both the -0.25 Hf and -1.0 Ta containing alloys are stronger than the binary material at the smaller samples sizes.

However, the figure also illustrates that the strengthening effect from reducing the sample diameter outweighs the strengthening from changing the alloy composition in all cases. Finally Fig. 2 shows the normalized average 1 % offset shear flow stresses versus microcrystal diameter, together with comparisons to pure Ni from other studies [12]. The flow stress data are shown normalized by the anisotropic shear modulus and Burgers vector ratio since the strength of dislocation sources scales by these quantities. Also, for each alloy the macroscopic crystal flow stress, τ_o, is subtracted so that the strengthening from changes in sample diameter shows clearly. Note that the Ni_3Al alloys strengthen to a greater degree as a function of their size than similarly prepared pure Ni microcrystals that are representative of the FCC class of materials. Further, the influence of microcrystal size is also more potent (steeper slope). For the Ni_3Al alloys, the figure indicates that the flow stress tends toward a saturation value for samples < 2 μm diameter. For comparison, as discussed later, the plot also shows the stress range for instability of incomplete KWL and complete KWL by athermal cross slip given by Caillard and Paidar [22], and the range of stresses necessary for the superpartials to glide as separate single dislocations.

Slip Traces and Glide Bands

SEM images of deformed microcrystals corresponding to some of the stress–strain curves of Fig. 1 are shown in Fig 3. While not all of the deformed samples can be shown, notable trends were found as evident in the images shown. First, there is a trend that larger diameter samples *tend* to exhibit more homogeneous slip bands, while smaller samples exhibit more isolated slip traces. Also, the -0.25 Hf alloy that forms KWL at room temperature to a greater degree than the binary material, also shows the homogeneous banding at smaller sample sizes. When compared to the slip traces from pure Ni microcrystals, the Ni_3Al microcrystals show slip bands having an extremely uniform slip trace distribution within the bands and, a tendency toward more singular intense-strain slip traces at small diameters. Surprisingly and especially for the -0.25 Hf and -1.0 Ta alloys, these characteristics have little relationship to the characteristics of the stress-strain curves. That is, for all alloys at crystal sizes larger than ~2 μm, the samples show strengthening at small strains followed by nearly instantaneous large bursts and slip-band thickening, while the small crystals show similar strengthening and large strain bursts without slip-band thickening.

To gain further insight into the strengthening and deformation mechanisms, selected samples of the binary and -0.25 Hf alloy were loaded to stresses below the breakaway flow stress, unloaded and, examined via SEM and TEM imaging. One such sample is shown in Fig. 4 together with the corresponding stress-displacement curve. Fig. 4a reveals that during the loading stage microstrain bursts occur over the period of exhaustion hardening, while the corresponding Fig. 4b shows that slip is primarily occurring on isolated single slip traces (to the degree they can be resolved), with essentially no slip-band thickening. Note that the image of Fig. 4b has been digitally enhanced to better view the extremely fine slip traces on the surface. Further, the glide events appear to involve dislocation processes that sweep the entire glide plane. Slip traces do not appear to end within the microcrystal, particularly for smaller sample sizes. Further, while not quantitatively shown, there is an approximate one-to-one correspondence between the offsets or strain bursts on the stress strain curve and the observed slip traces, indicating that dislocations are not multiplying in large numbers while the crystals strengthen by exhaustion.

However, once a sufficient stress is attained exhaustion ceases and flow proceeds by a rapid strain burst and glide-band thickening. To estimate the minimum number of dislocations that multiply and leave the crystal to form the glide band, consider the 5 μm -0.25 Hf microcrystal shown in Fig. 3c. The time series testing data indicates that forming the thick slip band corresponds to a platen displacement, ΔL, of ~1988 nm that was achieved in ~0.213 s, corresponding to an average platen velocity of v_p = ~9.3 μm/s. From geometry one may deduce that a shear displacement in the slip plane of ~2811 nm is required for such platen motion and a displacement of that magnitude corresponds to ~5567 superdislocations sweeping the full slip-plane area. Also from geometry, for such a 5 μm diameter sample a unit axial displacement corresponding to a single dislocation sweeping the glide plane, ΔL_b, in time $t_{\Delta L}$ implies that the dislocation travels a distance of ~2.16×10^4 times ΔL_b during that same time. Thus, a corresponding lower-bound dislocation velocity, v_d, may be estimated as ~36 μm /s. A similar estimate of the dislocation velocity during the formation of a slip trace that involves only ~4 dislocations resulted in a similar estimated value for v_d.

Transmission Electron Microscopy

Further understanding of dislocation mechanisms was achieved by selected TEM examinations of deformed microcrystals. Figure 5a shows a SEM image of a deformed 10 μm Ni_3Al-0.25Hf microcrystal, together with a schematic overlay of how the crystal was sectioned parallel to the loading axis for TEM examination. Figure 5b shows a bright-field scanning transmission electron microscopy image for the sectioned microcrystal revealing a high dislocation density in the glide band. While the base of the sample away from the slip zone shows relatively few dislocations after testing (measured density of $< 1 \times 10^{12}/m^2$), the upper portion of the image shows a clear concentration of stored dislocations occurring within the wide slip band. Within the band, the dislocation density has risen to $> 1 \times 10^{13}/m^2$, after about 9 % engineering strain indicating that deformation proceeds via relatively homogeneous multiplication and storage of dislocations. However, using the measured dislocation density in the slip band, a mean-field Taylor-type strengthening model estimates the flow stress at a value that is about one-half of the observed microcrystal flow stress.

Selected microcrystals were also studied using TEM foils oriented parallel to the primary slip plane within slip traces and bands. Images from two such cases are shown in Figs. 6 and 7. For the 5 μm diameter, Ni_3Al binary alloy sample shown in Fig. 6, a single slip trace is shown after deformation was stopped in the loading regime after only 0.9 % strain. The entire sample slip-plane cross section is shown in the bright-field image of Fig. 6a. Fig. 6b shows several KWL loops containing MK segments emanating from a surface source marked "S" on the image. For this sample, the dominant dislocation features are the KWL and MK that are common to the flow stress anomaly regime, even though the deformation was carried out at room temperature. Further, for macroscopic crystals of this alloy the room temperature deformation structure consists of non-screw character multi-pole braids, unlike the present structure [36, 45]. This observation suggests that the small sample dimensions promote screw-dislocation locking and/or, the mean glide distance for non-screw dislocations (MK) exceeds the sample dimensions. Weak-beam dark-field imaging of the same features (Fig. 6c) better reveals the parallel glide loops in this slip trace. Close examination of the image indicates that fine elongated intrinsic stacking fault (ISF) loops exist lying parallel to KWL segments. Also, the image of Fig. 6d formed using an imaging vector that places the superpartial dislocations out of contrast, reveals residual APB tubes and ISF loop contrast. Note that the APB tube that has been marked extends across the entire span of the image in a crystallographic straight fashion.

Figure 7 shows a similar slip-plane section for a 5 μm diameter Ni_3Al-0.25Hf alloy microcrystal but, this time the TEM foil was extracted from a thick glide band formed while the sample experienced a large 15.7 % engineering strain burst. The burst took place under a constant engineering stress of 538 MPa in less than 0.4 sec. The bright-field image of Fig. 7a shows a unique dislocation structure for this Ni_3Al alloy that has not been reported by any of the prior studies. For modest strains and deformation strain rates, this alloy commonly exhibits extensive KWL dislocations at room temperature and comparatively few multi-pole braids by comparison to the binary alloy [37, 46]. However, for this microcrystal the dislocation structure exhibits a dual nature consisting of both extensive KWL/ISF loops (dark features marked "ISF") and extensive multi-pole braid regions that on Fig. 7a show as several dense bands (marked "MPB" on the image). The higher magnification weak-beam dark-field image in Fig. 7b of the region marked by white lines in Fig 7a clearly resolves the KWL/MK as well as the multi-pole braid configurations.

DISCUSSION

The results of this study leads to questions pertaining to both small-sized crystal effects and, the relationship between microcrystal and macroscopic crystal responses. For example, how are the dislocation mechanisms for Ni_3Al macroscopic crystals relevant to microcrystal response? Does the microcrystal response lend further insights into the micromechanisms operating in bulk Ni_3Al? Why do the Ni_3Al alloys exhibit a greater relative strengthening as a function of microcrystal diameter when compared to other materials? Why do microcrystals of a wide variety of materials show so many common attributes, irrespective of their crystal structure and, why do the Ni_3Al alloys show the same consistent features even though the fundamental dislocation mechanisms (namely KWL and MK formation) are unlike any of the materials examined in prior studies? Our discussion proceeds from these queries.

Key Observations

Macroscopic Ni_3Al Dislocation Mechanisms

To begin, consider the following facts, primarily from macroscopic crystals of the same Ni_3Al-binary and Ni_3Al-0.25Hf alloys examined here. From prior studies, especially from Shi, et. al. [37], reports show:

1. Both the binary and Ni_3Al-0.25Hf alloy exhibit screw-character KWL dislocation configurations after room-temperature deformation; however, they are relatively infrequent for the binary materials and are more prevalent for the Ni_3Al-0.25Hf and Ni_3Al-1.0Ta alloys. This result and the stress-strain data indicate that the Hf- and Ta-containing alloys are in the anomalous-behavior deformation regime at room temperature [36-38]. The higher fault energies for these alloys (Table I), especially those for Γ_{csf}, lead to this behavior.

2. Studies of Ni_3Al alloys show evidence that mixed- and near-edge-character dislocations contain jogs that locally provide weak pinning points on the dislocation segments [37, 47, 48]. Further, since the non-screw character dislocations (MK) do not show significant local cusps and since the macroscopic strain-rate sensitivity of the material is low, the jogs are primarily glissile. This observation also suggests that *double cross slip* occurs over dimensions comparable to the KWL heights out of the glide plane [48].

3. For Ni_3Al-0.25Hf, the spacing of screw dislocations normal to their line direction is large by comparison to MK or KWL structures, being a few microns at its maximum. This feature is true when considering both the TEM images of projected segments and for tilting experiments that lend insight into the 3-dimensional nature of the structures. Also, the deformation microstructures contain many dipole loops that are aligned with the ends of screw segments and extend obliquely to the screw lines. The results suggests that the glide distances for screw-charter dislocations are on the order of the observed spacing and, that cross slip anni-

hilation of dislocations is prevalent [46, 48].

4. For the cases where the heights of the MK that join the KWL segments were measured, they were shown to form a distribution at small sizes (peaked at < ~10.0 nm) [22, 37, 49]. While MK likely propagate slip along the KWL segments contributing strain, both their dimensions and numbers are small relative the mobile dislocation density required to propagate slip to large strains—that is, multiplication and annihilation mechanisms are required to result in the observed structures. Thus, sources and/or the accumulation of MK are needed, together with long glide distances parallel to the KWL for significant strain to accumulate by MK motion alone. Taken together with evidence in # 2 and # 3, these point toward a 3-dimensional, yet primarily planar slip with double cross slip over short distances in the cubic plane [46].

5. Slip traces are known to be planar, finely spaced, extending over distances of several micrometers at low temperature and, exhibit heights of only a few Burgers vector magnitudes, as revealed by both in situ and post mortem atomic force microscopy observations of the surfaces of deformed macroscopic crystals [50, 51].

6. Shi, et. al., report that APB tubes form in numbers comparable to the occurrences of KWL segments, being dragged out from near-edge character dislocations. The tubes have perfect straight-line lengths, even more adherent to the <110>-type screw dislocation directions than the KWL themselves (because of MK). Importantly, the tubes extend continuously over distances of many micrometers (> 5 μm), whose upper bound is limited by the dimensions of the TEM foils [23, 37, 52].

7. Shi, et. al., also report that the lengths of the KWL segments connected by MK are shorter than those of the APB tubes, by an order of magnitude or more. The lengths of the KWL segments only rarely approach 1 μm [24, 37].

8. The stress-velocity relationship as a function of temperature for individual dislocations, exhibits the characteristics of the flow stress anomaly [53, 54]. Both the effective stress

needed for motion and the stress sensitivity of the dislocation velocity, increase with increasing temperature.

The features are schematically depicted in Fig. 8 to give a sense of them in the context of Ni_3Al microcrystals. Figure 8a shows a slip plane in a microcrystal together with a dislocation loop drawn to approximately the relevant scale and orientation of the microcrystal experiments. A larger view of the same dislocation loop is shown in Fig. 8b having the key features identified. Collectively, these features are evidence to suggest that the 'mean-free-path' or average glide distance for non-screw character dislocations is larger than the specimen diameter or slip-plane dimension for many of our microcrystals. The same is likely true in the direction normal to the screw direction for the smaller crystals of the present study. The consequences of this are reflected in the key attributes of the deformed microcrystals described next.

Deformation Features of Microcrystal Ni_3Al

Next, we consider and compare the following key observations from the present microcrystal deformation studies.

1. Strengthening versus sample diameter is more potent for Ni_3Al alloys than for FCC metals (Ni), even after shear stresses are normalized by the material shear modulus and Burgers vector magnitude (Fig. 2).

2. Microcrystals of all sizes below ~20 μm achieve their maximum strengthening during a microstrain loading interval that typically ends after ~0.5 % engineering strain. For these crystals the loading interval is followed by a relatively catastrophic flow burst.

3. For the -0.25 Hf and -1 Ta containing alloys, crystals of all sizes show breakaway flow bursts after the initial exhaustion interval. For the binary alloy, samples having diameters larger than ~10 μm sometimes show rapid flow bursts, and at other times exhibit the stair-stepped like avalanche behavior that is common to microcrystals of other materials (Fig. 1a).

4. Loading proceeds via exhaustion of mobile dislocations, as indicated by microstrain bursts, an exceptionally high hardening rate at small strains and, TEM observations of slip traces such as shown in Fig. 6. During this loading interval, the samples form isolated narrow slip traces that are well separated from each other even for large diameter crystals (Fig. 4).

5. TEM examination of a 5 μm diameter binary alloy sample shows that during room-temperature loading, dislocations form the KWL and ISF loop structures while leaving residual APB tubes (Fig. 6).

6. The large strain bursts that characterize flow, proceed over short time intervals (~0.2 s) during which the strain rate increases from a nominal rate of 10^{-4}/s to average values in the range from 1 - 10/s; that is, a change in the effective strain rate of 10^4 to 10^5/s (not shown).

7. For sample diameters less than ~2 μm, slip traces often do not thicken during the large strain flow bursts. For larger samples, flow leads to slip trace thickening into uniform glide bands having a homogeneous distribution of slip.

8. At sample diameters greater than ~2 μm, the dislocation structure formed during rapid glide-band thickening contains both KWL/MK/ISF and multi-pole braid dislocations, both at a high stored density.

9. The estimated lower bound of the dislocation velocity during these flow bursts is on the same order as that measured for isolated dislocations in macroscopic crystals, but at higher apparent applied stresses.

Comparing the two sets of observations generally suggests that while the individual dislocation mechanisms of Ni_3Al alloys are preserved for deformation of microcrystals, the mean-field mechanisms of dislocation multiplication, glide and locking that set the levels of stress are severely disrupted. The small crystal dimensions do not permit the same dislocation multiplication rates at the same stresses as for macroscopic crystals. *Consequently, stress is the primary free variable that adjusts to higher levels to activate processes necessary for sustaining flow at the prescribed rate.* Further, the primary mechanism of dislocation multiplication for FCC materials (and perhaps for their derivatives such as Ni_3Al) is double cross slip. Thus, for Ni_3Al microcrystals, it is important to understand not only the relationship between cross-slip and locking of screw dislocations, but also unlocking and double-cross-slip multiplication.

Size Effect Strengthening

Figures 1 and 2 show that the specimen-size dependent strengthening of Ni_3Al alloy microcrystals is qualitatively consistent with prior microcrystal studies indicating that strengthening occurs by exhaustion of the mobile dislocation density during the first few percent of plastic strain because dislocations cannot readily multiply. However, for Ni_3Al alloys, the exhaustion processes are more potent since the pre-plastic flow strains are typically less than ~0.5 %, versus up to ten times that level for FCC Ni microcrystals. While not shown here, comparisons to literature data indicate that the strengthening by size-related micromechanisms is even greater than the strength rise over the regime for the flow-stress anomaly to its peak strengthening [33]. Further insights are obtained from the results of interrupted microcrystal deformation tests as shown in Figs. 4 and 6. The strengthening occurs after plastic processes have started but prior to the necessary conditions for dislocation multiplication. The single-trace slip events shown in the figures indicate glide of mixed segments or MK, together with glide of screw-character dislocations by some means (full loops), such that full slip planes are swept during loading. These slip events at vanishingly small thicknesses suggest the action of single slip plane sources that propagate to exhaustion with no significant multiplication.

Just as for FCC metals and other materials, such high strengths can only be achieved by exhausting the supply of mobile dislocations at a given stress. For Ni_3Al microcrystals there are several ways to exhaust the mobile dislocation density that are accentuated by the reduced sample size. For example, the anisotropic elastic interaction between the superlattice partial dislocations and the APB energy anisotropy continue to provide ample driving force for cross-slip locking of dislocations in microcrystals. However, both the small crystal dimensions and the presence of free surface may accentuate this exhaustion process. The finite crystal size limits flow processes to length scales below the mean-free-path for multiplication (MK leave the crystal before multiplying). Further, free surfaces are known to promote cross-slip [55], which for Ni_3Al alloys may bias the screw-character dislocations toward a higher fraction of complete KWL segments per unit time, effectively substituting for temperature in promoting the locking process. Since the single-arm dislocation source model has been so effective in describing the behavior of FCC microcrystals, a similar (though phenomenological) model is considered here for these surface-enhanced exhaustion processes.

Surface Cross Slip and Single-Arm Dislocation Sources

As discussed in the Introduction, one mechanism previously shown for strengthening of FCC microcrystals is dislocation source truncation to form single-arm dislocation sources. Such a model may be justified for Ni_3Al microcrystals based on the expected enhanced dislocation exhaustion mechanisms and the observations of localized strain accumulation on isolated slip traces for the smallest microcrystals (see Fig. 3a and b). When dislocation segments meet the free surface, surface cross slip may immediately lead to KWL formation (complete or incomplete). We consider a model that is based on glide proceeding via MK sources that intersect free surfaces but, also encounter some obstacle that pins one end within the crystal, such as the low mobility cubic plane jog segment that connects complete KWL and MK segments. The model follows from the one by Demura, et. al., for macroscopic Ni_3Al crystals [56]. Thus, we assume that for microcrystals the rate of KWL formation is enhanced and becomes a function of the sample size. Since locking is enhanced by surface cross slip the MK height distribution shifts to smaller values for smaller crystals. For these conditions, the yield stress is given by the stress to operate a source based on its length, which in this case is the MK height, l_c, giving the shear stress as

$$\tau = K_s b / l_c \tag{1}$$

Following Demura, et. al., the MK height is given by the free-flight velocity of dislocations or

$l_c = v/f$ where f is a cross slip frequency [56]. The velocity of the screw dislocations becomes $(\tau - \tau_i)b / B$ where B is a drag coefficient and τ_i is an internal stress, in this case written as

$$\tau_i = K_s b / \beta R + 0.35 K_s (\rho_{total})^{1/2} + \tau_{ss} \qquad (2)$$

In Eqn. (2), βR represents the average length of a single-arm source [6] expressed as a fraction of the sample radius R, ρ_{total} is the dislocation density and τ_{ss} is a solid-solution hardening stress. The second term in Eqn. (2) represents a forest hardening contribution. Solving for the microcrystal flow stress, one obtains

$$\tau = [\tau_i + (\tau_i^2 + 4K_s Bf)^{1/2}] / 2 \qquad (3)$$

Again following Demura, et. al., the frequency of cross slip on a source of length βR becomes

$$f = f_o[(\beta R - \delta) + C\delta] / \beta R \qquad (4)$$

where f_o is the macroscopic crystal cross-slip frequency, C is a surface cross slip amplification factor given as

$$C = exp[-(\Delta H_s - \Delta H_b) / kT] \qquad (5)$$

Where ΔH_s and ΔH_b are the activation energies for cross slip at surfaces and in the bulk, respectively and kT has its usual meaning. In Eqn. (4), δ is a measure of the 'surface region', that leads to the only free parameter in the model as the product, $C\delta$, that represents the potency of surface cross slip.

Figure 9 shows the result of this surface cross slip model for parameters taken to describe binary Ni_3Al alloy as shown in the figure caption. While the explicit details and mechanisms of the model cannot be shown or isolated in experiments, the figure suggests that such a model does represent the 0.2 % stress that is experimentally observed before breakaway flow. This suggests the role of surfaces on enhancing exhaustion is a possible mechanism for the rise in flow stress over the loading regime, though the mechanism for forming dislocations needs further elucidation. Unfortunately, the pathway from a model for strengthening at small strains, to a mechanism-based model for the breakaway flow is less clear.

Strength Saturation, Dislocation Multiplication & Breakaway Flow

By comparison to the macroscopic crystal case, what is missing for Ni_3Al microcrystals is a ready supply of dislocation sources to offset the enhanced locking and exhaustion processes. Yet, once some critical stress is achieved for the given microcrystal size, such a source is triggered and profuse dislocation multiplication and flow proceeds that generates many thousands of mobile segments while forming uniform thick glide bands in the larger crystals (Fig. 3d and 3f). Many of the microcrystals, especially the larger ones and the ones in alloys containing -0.25 Hf and -1.0 Ta, show fine homogeneous slip bands (Fig. 3f). For these the slip trace spacing is so small and fine that the crystals appear as though they were kinked, not deformed by glide, yet the TEM images of Figs. 5-7 indicate dislocation flow. Clearly, a critical stress for dislocation multiplication sets a limit on the strengthening obtained for a given crystal and distinguishes the pre-plastic loading and exhaustion processes from flow.

For macroscopic crystals, current understanding indicates that athermal double cross-slip unlocking of incomplete KWL provides a ready source of MK segments necessary to propagate flow. However, for microcrystals that strengthen to levels that exceed the Caillard-Paidar stress for incomplete KWL stability (Fig. 2), the supply of dislocations is more limited at a given stress. As mentioned previously, the strengthening effect shown in Fig 2 shows a tendency for saturation at sample sizes below ~2 μm for stresses at the upper limit of complete KWL stability. Thus, to explain the critical stress and occurrence of breakaway flow, it is useful to examine the dislocation mechanisms described by Caillard and Paidar and their model for the flow stress anomaly based on exhaustion processes. They proposed that glide proceeds through athermal cross-slip *unlocking* of KWL [22, 23, 33]. In this model the occurrence of the peak temperature for strain hardening by the flow anomaly mechanisms, $T_P(\theta_{max})$, is related to the onset of athermal unlocking of incomplete KWL. The threshold stress, τ_i, for this unlocking was derived as

$$\tau_i = \frac{\Gamma_{111}}{b}\left[1 - \frac{\Gamma_{100}}{\Gamma_{111}}\frac{1+2/A}{\sqrt{3}}\right] \approx 0.26\frac{\Gamma_{111}}{b} \tag{6}$$

where Γ_{111} and Γ_{100} are APB energies in the octahedral and cubic planes, respectively, and A is the elastic anisotropy factor ($2C_{44}/(C_{11}$-$C_{12})$, where C_{ij} are the elastic constants). From the values of the fault energies given in Table I together with Eqn. (6), one may estimate the threshold stress for the beginning of incomplete KWL breakdown. That stress for binary Ni_3Al alloy is indicated by the lower bound (red solid line) of the horizontal shaded region on Fig. 2.

Further, should the KWL be fully extended on the cubic planes, the model derived an upper bound, above which complete KWL are athermally unstable given as

$$\tau_i = \frac{\Gamma_{111}}{b}\left[1 - \frac{\Gamma_{100}}{\Gamma_{111}}\frac{1}{\sqrt{3}}\right] \approx 0.54\frac{\Gamma_{111}}{b} \tag{7}$$

and that stress value is indicated by the upper bound (cyan solid line for the -1.0 Ta alloy) of the shaded region on Fig. 2. However, that the experimental microcrystals appear to show strengthening saturation at stresses that lie above even this line for the upper and lower bound of the model (Fig 2). To explain this we suspect that dislocation-dislocation interactions could lead to local stresses that are in the range given by Eqns. (6) and (7), even though the applied stresses are much lower, leading to double cross slip and screw-character dislocation propagation for larger microcrystals that never attain applied stresses that exceed the Caillard-Paidar model lower bound. For this to occur, 'pile-ups' of screw-character dislocations must occur on the glide planes (or closely spaced glide planes). Such effects may govern the breakaway strain intervals in the larger microcrystals after a period of exhaustion hardening.

Consequently, the picture that emerges for the size-affected behavior of microcrystals is as follows. For larger crystals, sources operate and exhaust by KWL formation, MK propagation and depletion at free surfaces and, by the single-arm source processes expected for Ni_3Al alloys. As stresses rise during exhaustion, the interactions between stored KWL segments amplify the applied stress locally, eventually leading to athermal breakdown of the locks leading to double cross slip, rapid dislocation multiplication, dissipation of the local interaction stress and large strain events. Provided the crystals are large enough for interaction stresses to build and release in repeated avalanche cycles over some strain range, the process leads to the stair-stepped flow curves as shown in Fig. 1a. Such a conceptual process is schematically depicted by the dislocation configuration in Fig. 10.

Examination for Fig. 10 indicates that an additional limiting mechanism needs consideration at the limit of KWL stability. Since the heights of KWL segments range from ~0.5 to 6 nm, once double cross slip sources are formed expanding loop segments will experience strong dipole (multi-pole) interactions at the screw-character positions (see "dp-" and "dp+" points on Fig. 10). For these segments to persist as sources, the local stresses must permit passing of the interacting dipole segments at critical heights that are in the range of the KWL partial dislocation separation distances. The critical dipole height, h_c, that can be passed as a function of stress has been estimated from elasticity theory and is shown on Fig. 11, together with estimates of the critical MK segment heights, l_c, that can be activated at a given stress. The stress range for incomplete KWL and complete KWL stability (as shown on Fig. 2) and, the typical stress range for 20 μm diameter Ni_3Al alloy microcrystal flow stress are also shown. As Fig. 11 shows, estimates for the screw-dipole passing stress for dipoles having the complete KWL height are much larger than the applied stresses for larger microcrystal sizes. Thus, for the superdislocation double cross slip dipole-crossing concept to hold, dislocation interactions that enhance the local stress appear to be needed, such as the interactions that would form between points A, B and C in Fig. 10.

As crystal sizes diminish, interaction stresses are more difficult to achieve and the applied stress must substitute to achieve the dipole-passing stress. For these conditions, stresses rise into the saturation regime where the applied stress leads to complete KWL and glide proceeds in a manner that is analogous to the behavior of FCC metals, provided that surface cross slip and dislocation interactions do not overwhelm even these processes. Such conditions occurring during breakaway flow are primarily responsible for the dual nature of the observed dislocation substructure and the transition from thick glide bands to intense shear slip traces at small sample dimensions.

Finally, for the smallest crystals where exhaustion processes are at a maximum, it is possible that the superdislocations themselves are unstable and break away flow proceeds by uncoupled superlattice partial dislocations behaving as single-arm sources (see shaded region between dashed lines in Fig. 2). The result is extremely planar shear and glide bands that do not thicken (Fig. 3a - b).

For comparison purposes, Fig. 12 shows the measured individual dislocation velocities as a function of effective stress at varying temperatures for macroscopic binary Ni_3Al alloy single crystals [53, 54]. That prior work demonstrated that the key attributes for the flow stress anomaly are exhibited by the individual dislocation behavior since the velocity versus stress curves show both an increasing slope and a shift to higher stresses with increasing temperature. Since the data for 81 K and 295 K intersect at a stress that corresponds very nearly to the macroscopic crystal flow stress at 295 K, the data imply that for the binary alloy, dislocation locking begins at or above room temperature. Further, the measured dislocation velocity at this cross-over stress is ~5 μm/s, that is of the same order as the dislocation velocity estimated for the 5 μm microcrystal during glide band thickening at room temperature. Note however that the macroscopic crystal stress leading to this velocity does not correspond since the microcrystal glide band forms at a much higher applied stress. The result implies that the estimated values for v_d in microcrystals given previously are likely underestimated. These values of v_d can only be lower bounds since the dislocations essentially have no inertia, while the platen of the testing device is surely influenced by inertia, but unfortunately in an unknown way.

Capsule Remarks

Returning the questions from which the discussion opened, the following insights are offered. The descriptions indicate that not only are the dislocation models for bulk Ni_3Al relevant to microcrystals, but also new insights into the importance of KWL stability and motion are shown from the microcrystal behavior. The microcrystals exhibit the same dislocation mechanisms as those for macroscopic crystals but, the truncated glide lengths associated with the mean-field dislocation dynamics forces the stress to increase to re-scale the processes to the finite glide distances available. The same types of effects occur for other materials where the finite sizes limit the free-segment lengths of the mean-field forest, thus leading to size-affected strengthening or “mean-field breakdown.” Thus, many materials exhibit a ‘size effect’ regime where the length scales of the dislocation processes are similar and lead to similar strengthening. Finally, the Ni_3Al alloys exhibit a greater strengthening as a function of microcrystal diameter when compared to other materials for at least three reasons. First, the super-dislocations have higher energies than ordinary ones leading to higher bowing stresses for similar-sized dislocation sources. Second, the small specimens and free surfaces enhance KWL formation and MK exhaustion thereby limiting the MK size distribution and the ability of dislocations to multiply. These limit the length of sources at a given dislocation density relative to FCC metals. Third, the nanometer scale dimensions of the KWL/MK configurations leads to strong dipole barriers once stresses are high enough for athermal cross slip unlocking (MK formation) at the stress limit of KWL stability.

SUMMARY & CONCLUSIONS

The present study examined the size-dependent strengthening for three Ni_3Al alloys via the microcrystal compression technique and the following attributes were found:

- Nearly all of the phenomenological attributes observed for other materials in microcrystal form were also observed for Ni_3Al alloys, even though the basic dislocation mechanisms are unique for this intermetallic material.

- The studies showed that size-dependent strengthening overwhelms the effects of varying alloy compositions (fault energy changes and solid-solution effects) and, extends at least to the stress limits of KWL stability.

- Deformation was characterized by two regimes: i) strengthening by dislocation exhaustion over a smaller strain range than for FCC alloys and, ii) breakaway flow. During exhaustion, only isolated slip traces form while during flow many dislocations readily multiply and glide bands thicken for samples greater than ~2 μm diameter. For smaller samples, flow is characterized by intense shear on isolated slip trace planes.

- TEM methods were used to examine the deformed crystals both at the stage of slip trace formation and during breakaway flow. Slip traces are characterized by KWL, MK segment, ISF loop and APB tube formation. Breakaway flow includes not only these attributes but also high densities of multi-pole braid formation.

- Time-series data were used to estimate the lower bound of dislocation velocity during slip trace formation and glide band thickening and yielded the same result of ~36 μm/s (but at different stresses) within experimental error. Together with the TEM results the data indicate that the dislocation mechanisms for microcrystals are the same as those for macroscopic Ni_3Al alloy crystals, but the stress ranges for their operation are re-scaled to higher values because of the small sample dimensions.

- While a specific quantitative model for strengthening and flow was not developed, a phenomenological model for strengthening by single-arm sources was shown to be consistent with the exhaustion-hardening measurements and, the observation of intense slip trace shearing at small sample sizes after exhaustion is exceeded. A conceptual mechanism for dislocation multiplication by cubic-plane double cross slip and dipole passing at the stress limit of KWL stability was introduced. The mechanism is a plausible means for explaining glide-band thickening and stair-stepped flow at the exhaustion-strengthening limit at applied stresses below the KWL stability limit for larger microcrystals.

We conclude that the concept and mechanisms of mean-field dislocation-ensemble breakdown remain as the best interpretation of microcrystal strengthening and flow responses. This includes strengthening by dislocation exhaustion mechanisms that are ultimately limited by achieving a critical dislocation multiplication stress that triggers the onset of flow, sometimes via avalanches. For Ni_3Al alloys, we speculate that the flow stress anomaly mechanisms and strengthening with increasing temperature are likely overwhelmed by size-dependent strengthening mechanisms, as very likely are the orientation dependencies, suggesting that the microcrystals may exhibit a normal temperature dependence of flow stress. Unfortunately, such speculations cannot be investigated with current day instruments.

ACKNOWLEDGEMENT

The authors are indebted to Ms. S.L. Kim and Dr. P. Sarosi assisting in the development of methods for TEM sample preparation. We thank Drs. T.A. Parthasarathy and Y-S. Choi for helpful technical discussions. We also acknowledge the Air Force Office of Scientific Research, the Defense Advanced Research Projects Agency and the Air Force Research Laboratory, Materials and Manufacturing Directorate for financial support. Finally, DMD offers a debt of gratitude to the late Dr. P. Veyssière, who provided a countless number of comprehensive discussions and insights over more than two decades regarding the myriad details of dislocation micromechanistic behavior in Ni_3Al alloys, as well as the -0.25 % Hf containing crystals used for this study. His professional presence in the community elevated the standard of performance for most in the field (including my own), while his personal friendship offered welcoming interactions on many occasions. He is sorely missed.

REFERENCES

[1] M.D. Uchic, P.A. Shade and D.M. Dimiduk, Ann. Rev. Mater. Res. 39 (2009) p. 361.

[2] J.R. Greer and W.D. Nix, Phys. Rev. B. 73 (2006) p. 245410.

[3] C. Zhou, S. Bulent Biner, R. LeSar, Acta Mater. 58 (2010) p. 1565.

[4] A.S. Budiman, S.M. Han, J.R. Greer, N. Tamura, J.R. Patel, W.D. Nix, Acta Mater. 56 (2008) p. 602.

[5] S.I. Rao, D.M. Dimiduk, T.A. Parthasarathy et al., Acta Mater. 56 (2008) p. 3245.

[6] T.A. Parthasarathy, S.I. Rao, D.M. Dimiduk, M.D. Uchic and D.R. Trinkle, Scripta Mater. 56 (2007) p. 313.

[7] H. Tang, K.W. Schwarz and H.D. Espinosa, Phys. Rev. Lett. 100 (2008) p. 185503.

[8] D. Kiener and A.M. Minor, Nano Lett. 11 (2011) p. 3816.

[9] S. Ho. Oh, M. Legros, D. Kiener and G. Dehm, Nature Mater., 8 (2009) p. 95.

[10] K.S. Ng and A.H.W. Ngan, Scripta Mater. 59 (2008) p. 796.

[11] J. Gil-Sevillano, I.O. Arizcorreta, L.P. Kubin, Mater. Sci. Eng. A 309-310 (2001) p. 393.

[12] D.M. Dimiduk, M.D. Uchic and T.A. Parthasarathy, Acta Mater. 53 (2005) p. 4065.

[13] B. Devincre, T. Hoc, L. Kubin, Science 320 (2008) p. 1745.

[14] J. El-Awady, M. Wen and N.M. Ghoniem, J. Mech. Phys. Solids 57 (2009) p. 32.

[15] V. Paidar, M. Yamaguchi, D.P. Pope and V. Vitek, Phil. Mag. A 45 (1982) p. 883.

[16] V. Paidar, D.P. Pope an V. Vitek, Acta Metall. 32 (1984) p. 435.

[17] B.H. Kear, Acta Metall. 12 (1964) p. 555.

[18] Y.Q. Sun and P.M. Hazzledine, Phil. Mag. A 58 (1988) p. 603.

[19] P.B. Hirsch, Phil. Mag. A 65 (1992) p. 569.

[20] G. Molénat and D. Caillard, Philos. Mag. 64 (1991) p. 1291.

[21] V. Paidar, G. Molénat and D. Caillard, Philos. Mag. 66 (1992) p. 1183.

[22] D. Caillard and V. Paidar, Acta Mater. 44 (1996) p. 2759.

[23] D. Caillard, Acta Mater. 44 (1996) p. 2773.

[24] P. Veyssière and G. Saada, in Dislocations in Solids, Vol. 10, edited by F.R.N. Nabarro and M.S. Duesbery (Elsevier, New York, 1996), Chapter 53.

[25] F. Louchet, Mat. Sci. Eng. A 234-236 (1997) p. 275.

[26] M.J. Mills and D.C. Chrzan, Acta Metall. Mater. 40 (1992) p. 3051.

[27] B. Devincre, P. Veyssière, L.P. Kubin and G. Saada, Phil. Mag. A 75 (1997) p. 1263.

[28] B. Devincre, P. Veyssière and G. Saada, Phil. Mag. A 79 (1999) p. 1609.

[29] T. Kruml, E. Conforto, B. Lo Piccolo, D. Caillard and J.L. Martin, Acta Mater. 50 (2002) p. 5091.

[30] Q. Qin and J.L. Bassani, J. Mech. Phys. Sol. 40 (1992) p. 813.

[31] Q. Qin, J.L. Bassani, J. Mech. Phys. Sol. 40 (1992) p. 835.

[32] A.M. Quitino and M. Ortiz, Mat. Sci. Eng A 170 (1993) p. 111.

[33] Y.S. Choi, D.M. Dimiduk, M.D. Uchic and T.A. Parthasarathy, Philos. Mag. 87 (2007) p. 1939.

[34] Y.S. Choi, D.M. Dimiduk, M.D. Uchic and T.A. Parthasarathy, Philos. Mag. 87 (2007) p. 4759.

[35] T. Kruml, J.L. Martin and J. Bonneville, Philos. Mag. 80 (2000) p. 1545.

[36] D.M. Dimiduk, Ph.D. Thesis, Carnegie Mellon University (1989).

[37] X. Shi, Thèse de Doctorat, l'Université Paris-Nord, France (1995).

[38] M.D. Uchic, Ph.D. Thesis, Stanford University (1999).

[39] S.J. Polasik, MS Thesis, The Ohio State University (2005).

[40] M.D. Uchic, D.M. Dimiduk, J.N. Florando, W.D. Nix, Science 305 (2004) p. 986.

[41] M.D. Uchic, D.M. Dimiduk, Mater. Sci. Eng. A 400-401 (2005) p. 268.

[42] P.A. Shade, R. Wheeler, Y.S. Choi, M.D. Uchic, D.M. Dimiduk and H.L. Fraser, Acta Mater. 57 (2009) p. 4580.

[43] D.M. Dimiduk, E.M. Nadgorny, C. Woodward, M.D. Uchic and P.A. Shade, Philos. Mag. 90 (2010) p. 3621.

[44] D.M. Norfleet, D.M. Dimiduk, S.J. Polasik, M.D. Uchic and M.J. Mills, Acta Mater. 56 (2008) p. 2988.

[45] C. Rentenberger and H.P. Karnthaler, Intermetallics, 16 (2008) p. 571.

[46] X.Shi, G. Saada and P. Veyssière, Philos. Mag. 73 (1996) p. 1419.

[47] C. Rentenberger and H.P. Karnthaler, Intermetallics, 11 (2003) p. 601.

[48] X. Shi, Saada and Veyssière, Philos. Mag. Lett, 71 (1995) p. 1.

[49] G. Molénat, D. Caillard and Y. Sun, Mater. Sci. Eng. A 164 (1993) p. 407.

[50] J. Fikar, C. Coupeau, T. Kruml and J. Bonneville, Mater. Sci. Engr. A 387-389 (2004) p. 926.

[51] C. Coupeau and J. Bonneville, Appl. Phy. Lett 90 (2007) p. 171914.

[52] X. Shi, G. Saada and P. Veyssière, Philos. Mag. 73 (1996) p. 1159.

[53] E. Nadgorny and Y.L Iunin, Proc. Symp. MRS 364 (1995) p. 707.

[54] E. Nadgorny, Unpublished Research.

[55] S.I. Rao, D.M. Dimiduk, M. Tang, T.A. Parthasarathy, M.D. Uchic And C. Woodward, Philos. Mag. 87 (2007) p. 4777.

[56] M. Denura, D. Golberg and T. Hirano, Intermetallics 15 (2007) p. 1322.

TABLE I

Alloy (at %)	a_0 (nm)	Primary slip system	b (nm)	Schmid factor	APB Γ_{111} (mJm^{-2})	APB Γ_{001} (mJm^{-2})	Fault Γ_{csf} (mJm^{-2})	Ref.
$Ni_{76}Al_{24}$	0.357	<110>{111}	0.505	0.467	176+/-27	135+/-18	206+/-27	[29]
Ni_3Al-0.25Hf	“	<110>{111}	“	“	185+/-20	165+/-20	235+/-40	[35]*
Ni_3Al-1.0Ta	“	<110>{111}	“	“	237+/-30	200+/-25	352+/-50	[29]$^+$

*Values interpolated from Fig. 12 of reference [35] so that direct comparisons are valid.

$^+$Values reported from N. Baluc and R. Schäublin, Philos. Mag. 74 (1996) p. 113.

FIGURE CAPTIONS

Figure 1. (a) Engineering stress-strain curves for single-slip oriented crystals of binary Ni_3Al ranging from 1-30 μm diameter. The dashed line shows the nominal shear strain-hardening rate (SHR) for the largest microcrystals as a fraction of the anisotropic shear modulus K_s. (b) Comparison of selected average engineering stress-strain curves for Ni_3Al, Ni_3Al-0.25Hf and Ni_3Al-1.0Ta. Sets contain averages from 2 - 6 samples at each size.

Figure 2 Comparison of shear flow strength, normalized by K_s, the macroscopic crystal shear flow stress and the Burgers vector ratio, versus sample diameter for the three Ni_3Al alloys, together with average values for pure Ni [12]. For comparison the plot also shows the binary alloy stress range for instability of IKWL (solid red line) and the -1.0 Ta alloy CKWL (solid cyan line) by athermal cross slip given by Caillard and Paidar [22]. Also shown are estimates of the stress range (upper shaded area bounded by the dashed red and cyan lines) necessary for the superpartials to glide as separated dislocations trailing APB fault.

Figure 3. SEM secondary electron images showing slip characteristics and overall deformation geometries for selected Ni_3Al alloy samples. (a) Ni_3Al binary, 1 μm diameter, 12 % engineering plastic strain; (b) - (d) Ni_3Al-0.25Hf, 2, 5 and 43 μm diameter, respectively and, 34.5, 16.4 and 5.5 % engineering plastic strain, respectively; Ni_3Al-1.0Ta, 0.5 and 20 μm diameter, respectively, and 54.2 and 10.1 % engineering plastic strain, respectively. Note the localization and planarity of shear in (a) and (b). Figure 3(c) shows a glide band used to estimate dislocation velocities discussed in the text. Figure 3(e) shows a severely deformed sample that included bending that occurs during the catastrophic glide burst. The inset in Fig. 3(f) reveals the homogeneous nature of slip trace that occurs for many cases in the larger samples.

Figure 4. Stress-displacement curve (a) and SEM image (b) of a 10 μm diameter Ni_3Al-0.25Hf microcrystal deformed near to the end of the exhaustion regime. The crystal was unloaded and slip traces were examined before the onset of the plastic flow regime. The image in (b) has been digitally enhanced via an edge-finding filter and levels adjustments to accentuate the visibility of the very fine slip traces. Note the approximate correspondence between number of offsets observed on the loading curve and the number of slip traces on the sample. Also note that the slip traces appear to traverse the entire sample diameter. This later finding was progressively more evident for smaller microcrystal sizes.

Figure 5. (a) Secondary electron SEM image of a deformed 10 μm Ni_3Al-0.25Hf microcrystal showing a thick glide band and a superimposed schematic TEM foil as sectioned parallel to the loading axis through the slip band. (b) Bright-field STEM image of the sectioned foil; black and white arrows indicate common positions of a slip trace and base of sample, respectively. The top portion above the black arrow shows a high dislocation density ($\rho_{total} \geq 10^{13}/m^2$) in the deformation slip zone, while the lower portion shows a lower dislocation density ($\rho_{total} \leq 10^{12}/m^2$) in the relatively un-deformed microcrystal base.

Figure 6. (a) Overall bright-field view of the slip plane trace of a 5 μm Ni_3Al binary alloy sample deformed to 0.9 % engineering strain. (b) Higher magnification view of a surface source near "S" that has emitted several loops. The dislocation loops contain Kear-Wilsdorf locks "KWL" and macrokinks "MK" marked on the figure. (c) Weak-beam dark-field image of the same region as shown in Fig. 6b showing dislocations in contrast. (d) Weak-beam dark-field image of the same region as shown in Fig. 6b showing dislocations out of contrast. Residual contrast is from intrinsic stacking fault loops and APB tubes.

Figure 7. (a) Bright-field TEM image of a 5 μm diameter Ni_3Al-0.25Hf sample showing nearly the entire primary slip plane extracted from a thick glide band. The sample was deformed to 24.7% total engineering plastic strain. The dislocation structure shows intrinsic stacking fault "ISF" loops as dark vertical contrast lines and dense multi-pole braids "MPB" aligned in near-edge configurations. (b) Weak-beam bright field image of region marked by white lines in Fig. 7a showing the KWL and MK fine structures existing together with the MPB structure.

Figure 8. Schematic illustration of a Ni_3Al microcrystal sheared on a single slip plane. The illustration shows a dislocation loop extending from a surface source. The loop expands in an anisotropic manner as the screw-oriented segments extend as KW locks joined by MKs. Loop expansion involves cross slip at dimensions comparable to the core width of the dislocation

which leaves jog debris that glides with non-screw character segments. The expansion also leads to APB tubes extending from the non-screw segments.

Figure 9. The predicted yield stress versus sample diameter for the Ni_3Al surface cross-slip (SCS) model described in the main text based on a size-dependent MK height. The plot shows the estimated 0.2 % offset flow stress as a function of the microcrystal diameter for the Ni_3Al binary alloy. Data (blue) are from experiments while the solid red line is for the model using $\delta = 10$ nm. Also shown are fine dashed lines for $\delta = 5.0$ and 20 nm and, a long dashed line (green) for the single-arm source model [6]. For the surface cross-slip model $\rho_{total} = 5 \times 10^{11}/m^2$, $C = 7000$ corresponding to an activation enthalpy difference of 0.2 eV and, $(K_sBf_o)^{1/2} = 0.0004K_s$

Figure 10. Because of anisotropic elastic interactions and APB energy anisotropy, a significant driving force for cubic-plane cross slip always exists. Once the KWL instability stress is exceeded, athermal cubic-plane double cross slip may occur on expanding superdislocation loops forming dislocation sources as shown by the schematic illustration. Only complete superdislocations are shown in the figure and segments of the {001} planes shown are disproportionately large for clarity. The spacing λ_c represents the average spacing between KWL segments. MK sources are formed by cubic plane double cross slip (hatched areas) and expand on closely spaced parallel {111} planes. Dipole segments are formed at the near screw-character orientations that may experience superpartial segment annihilation leaving dipole loop debris as shown, or form interacting superdislocation dipoles, dp^- and dp^+. For the dipoles to become sources, stresses must exceed not only the critical stress for activating MK segments of length, l_{MK}, but also the passing stress for a given height, h_c, which must be smaller than the complete KWL height since KWL segments form below the instability stress. Since the KWL heights are small as is the distance λ_c, dislocation interaction stresses at positions such as A, B, and C may locally amplify the applied stress to aide dipole passing.

Figure 11. Estimates of critical dipole crossing and MK expansion heights, h_c, and l_c respectively, as a function of shear stress; where $h_c = K_sb/[8\pi(1-\nu)\tau]$ and $l_c = K_sb/\tau$ ($K_s = 68.5$ GPa and $\nu = 0.33$). Estimates are shown in comparison to binary alloy incomplete KWL (lower bound) and -1.0 Ta alloy complete KWL (upper bound) instability stresses. The stress range that is typical for 20 μm diameter samples is also shown for comparison. The estimated stresses suggest that dislocation interactions are necessary to locally amplify the applied stress to attain dipole defeat for the larger samples. As the sample size decreases, stress amplification by interactions is less likely since the sample size limits interactions causing the applied stress to rise to achieve multiplication and plastic flow.

Figure 12. Measured dislocation velocities as a function of shear stress and temperature for the binary Ni_3Al alloy in macroscopic crystal form. The velocity was measured by standard techniques that include pulse loading of different durations at different stresses and consecutive selective dislocation etching after unloading to reveal the initial and final positions of dislocations [53]. The measurements were performed on the leading dislocations in groups (arrays or progressing slip lines) sometimes called 'dynamic pile-ups' moving from a light scratch. The horizontal line drawn at a dislocation velocity of ~5 μm/s marks the intersection point for the velocity-stress dependences at 81 K and 295 K. This velocity also corresponds to the typical onset of plasticity in many different materials. The finding is an agreement with the known temperature independent yield stress in Ni_3Al over this temperature range. At the same time, a strong anomalous (or "positive") behavior of such velocity-stress relationships is observed as temperature increases, again in agreement with the established temperature dependent of the yield stress in Ni_3Al. The anomalous behavior is also indicated by continuous shift of the $v(\tau)$ dependence to higher slopes (m) at higher temperatures, corresponding to an increase in the activation enthalpy from ~0.14 eV at 81 K to ~1.5 eV at 873 K.

Figure 1a

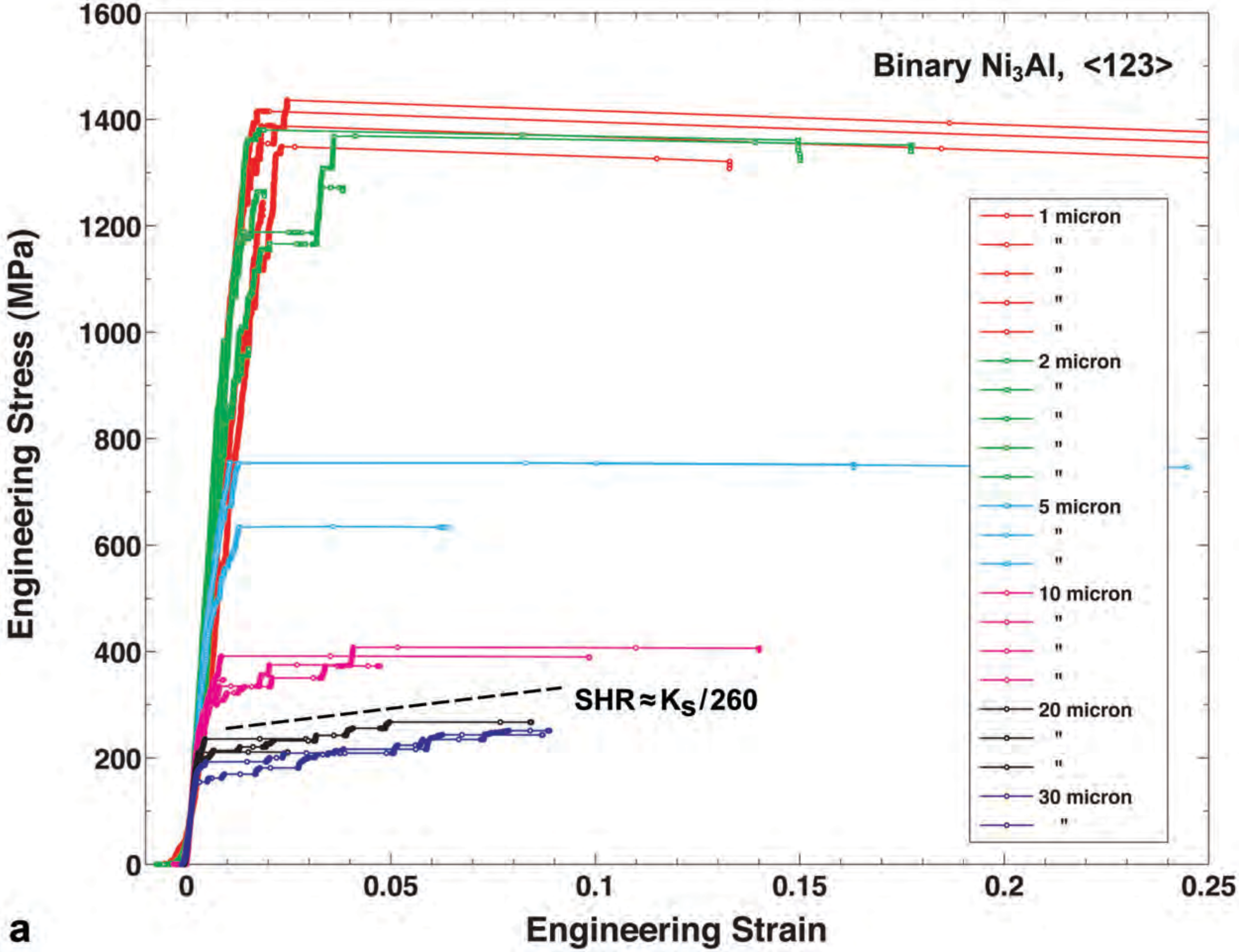

Binary Ni₃Al, <123>
1600
1400
1200
1000
800
600
400
200
0
Engineering Stress (MPa)
0
0.05
0.1
0.15
0.2
0.25
Engineering Strain
1 micron
"
"
"
"
2 micron
"
"
"
"
5 micron
"
"
10 micron
"
"
"
20 micron
"
"
30 micron
"
SHR≈K_S/260
a

Figure 1b

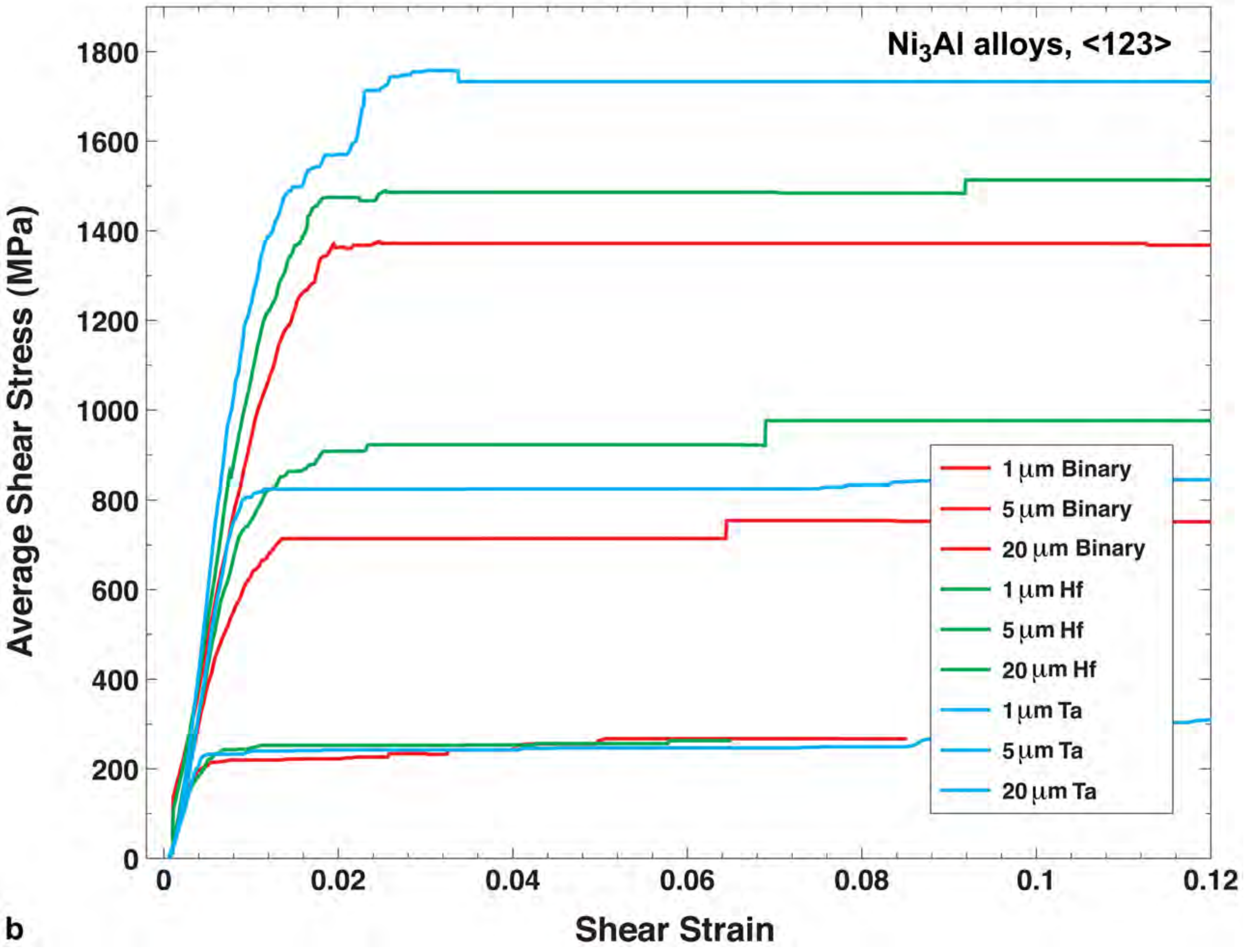
Ni3Al alloys, <123>
Average Shear Stress (MPa)
0
200
400
600
800
1000
1200
1400
1600
1800
0
0.02
0.04
0.06
0.08
0.1
0.12
Shear Strain
1 μm Binary
5 μm Binary
20 μm Binary
1 μm Hf
5 μm Hf
20 μm Hf
1 μm Ta
5 μm Ta
20 μm Ta
b

Figure 2

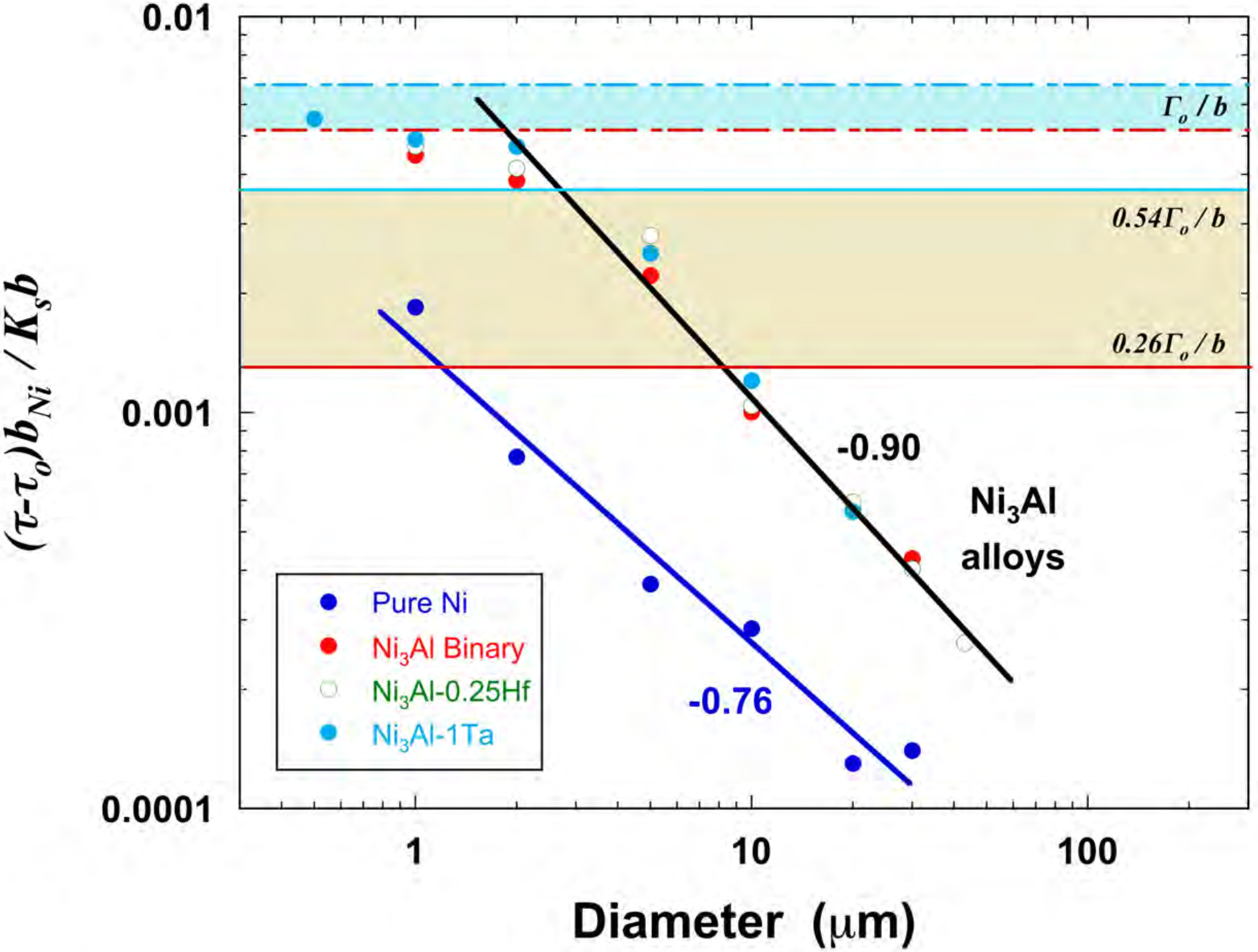
0.01
0.001
0.0001
1
10
100
Diameter (μm)
$(\tau-\tau_o)b_{Ni} / K_s b$
Γ_o / b
$0.54\Gamma_o / b$
$0.26\Gamma_o / b$
-0.90
Ni_3Al alloys
-0.76
● Pure Ni
● Ni_3Al Binary
○ Ni_3Al-0.25Hf
● Ni_3Al-1Ta

Figure 3

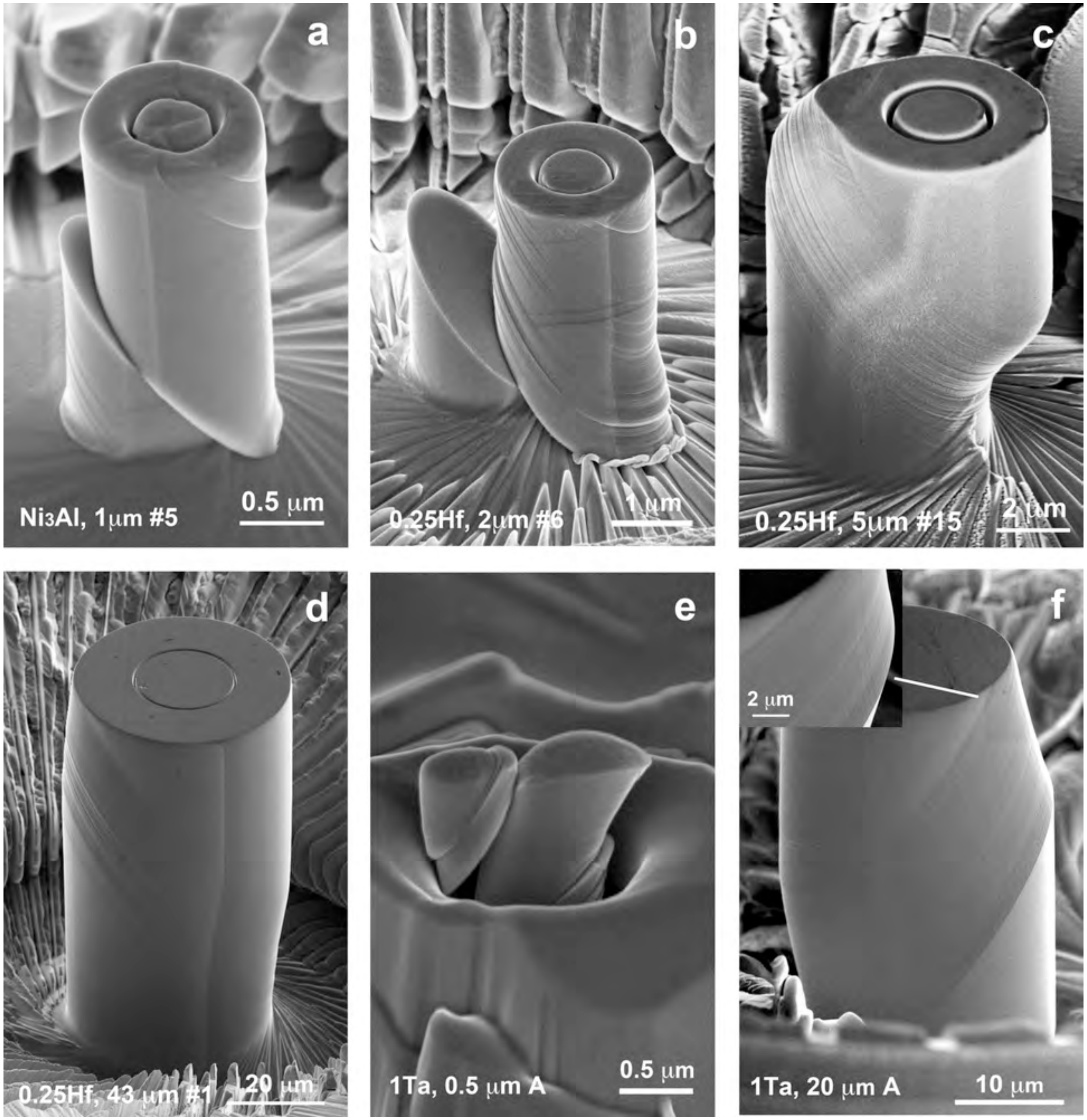
a
Ni3Al, 1µm #5
0.5 µm
b
0.25Hf, 2µm #6
1 µm
c
0.25Hf, 5µm #15
2 µm
d
0.25Hf, 43 µm #1
20 µm
e
1Ta, 0.5 µm A
0.5 µm
f
2 µm
1Ta, 20 µm A
10 µm

Figure 4

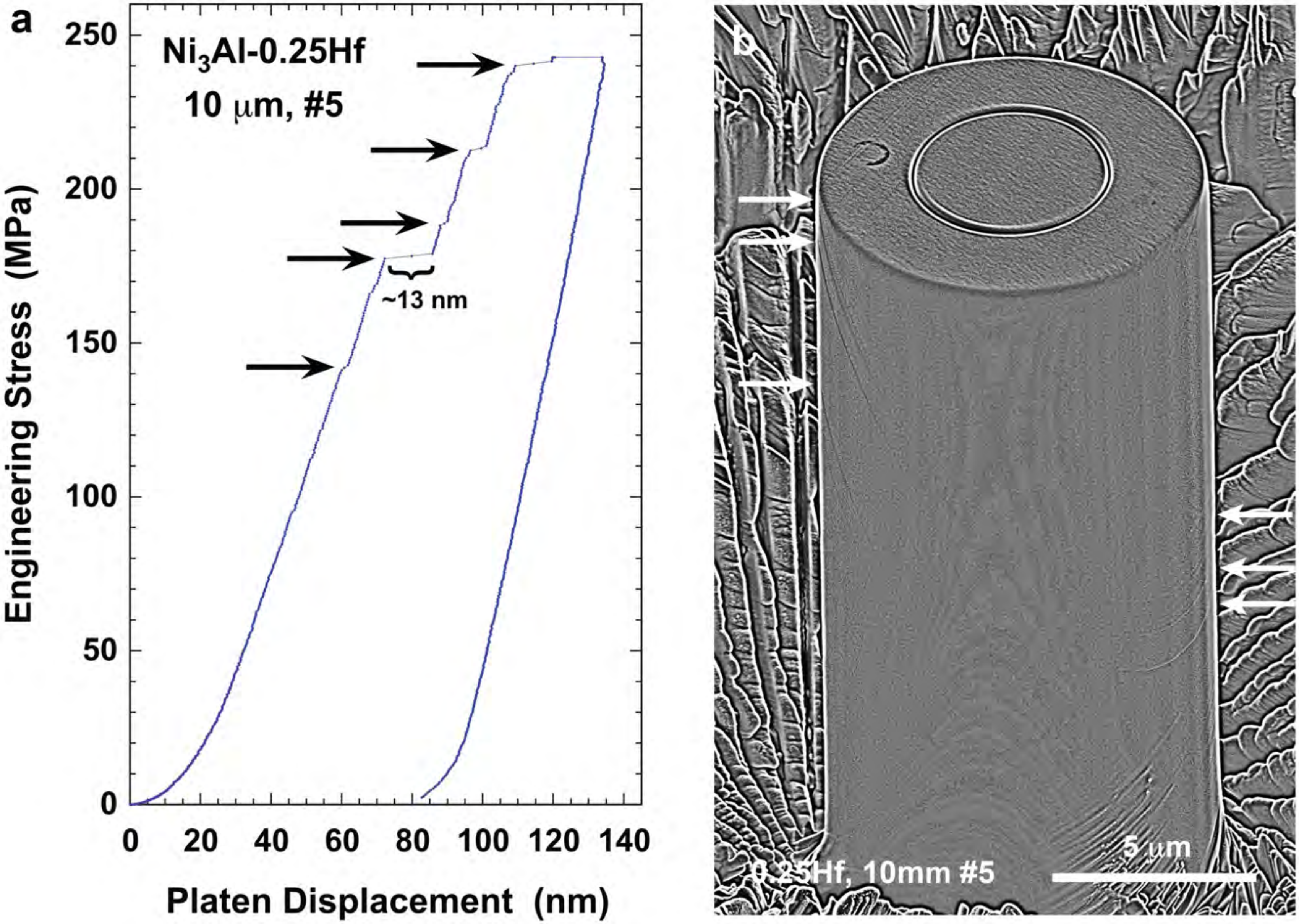
a
Ni$_3$Al-0.25Hf
10 μm, #5
~13 nm
Engineering Stress (MPa)
0
50
100
150
200
250
Platen Displacement (nm)
0
20
40
60
80
100
120
140
b
0.25Hf, 10mm #5
5 μm

Figure 5

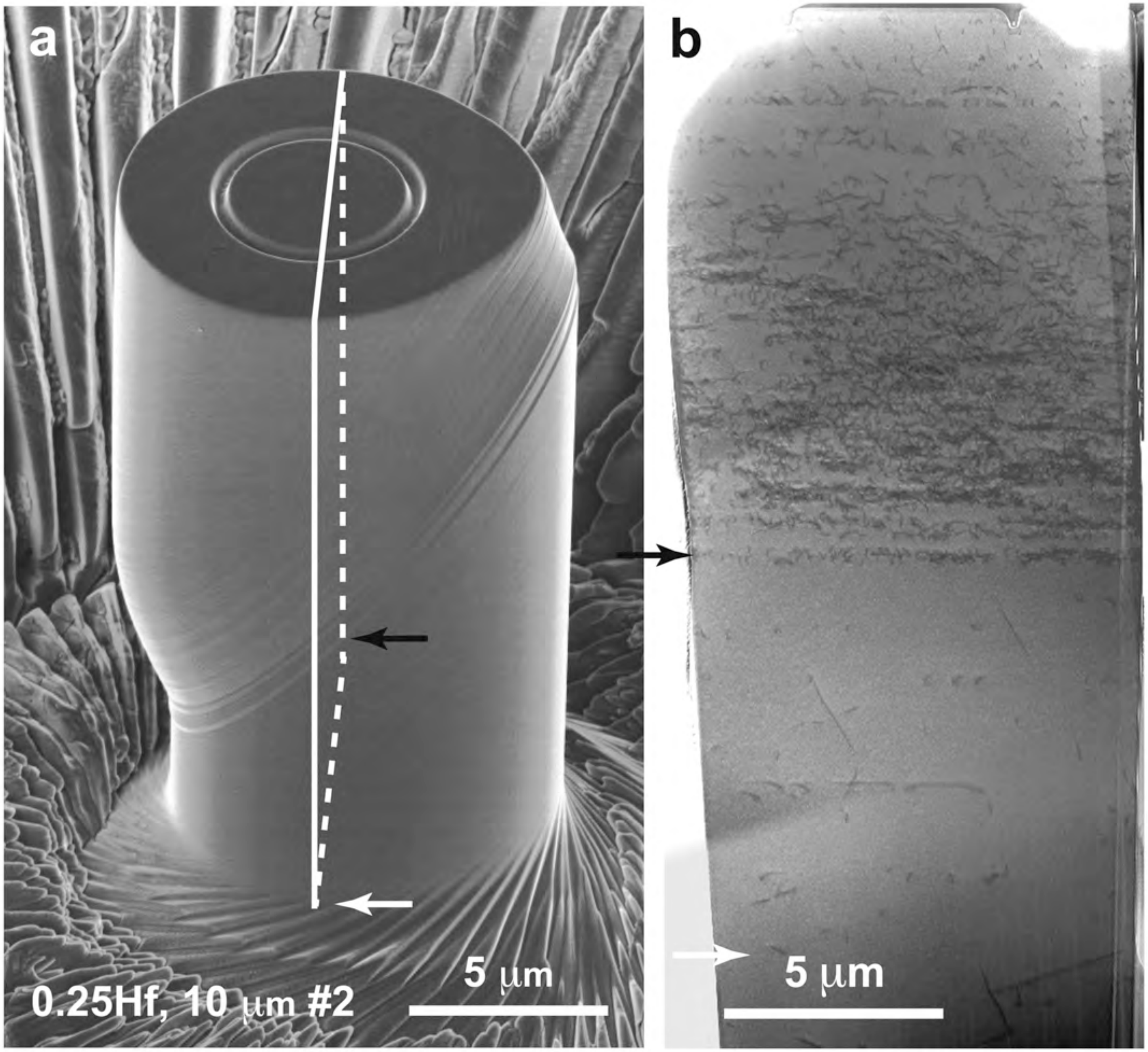
a
b
0.25Hf, 10 μm #2
5 μm
5 μm

Figure 6

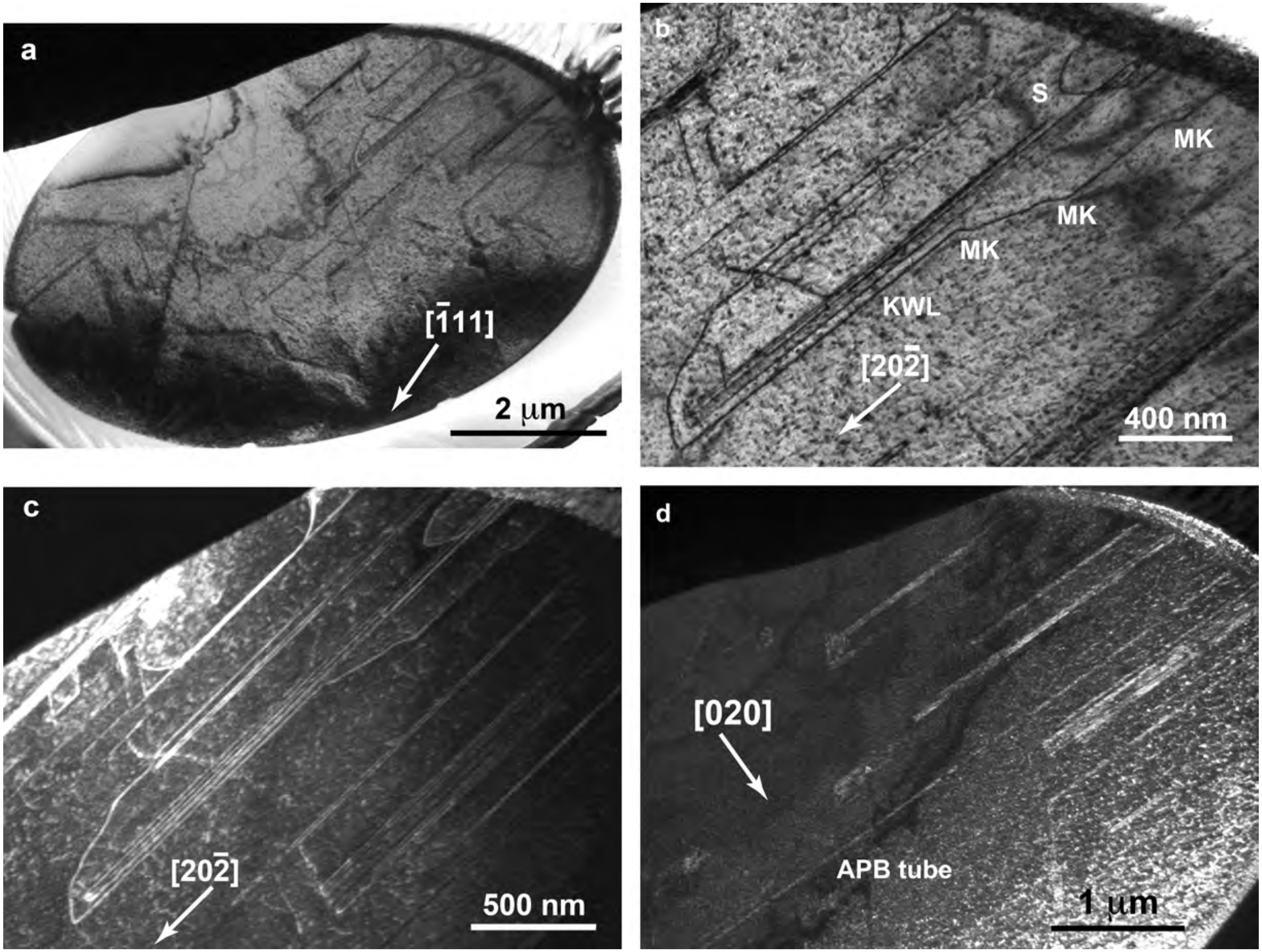
a
[$\bar{1}$11]
2 μm
b
S
MK
MK
MK
KWL
[20$\bar{2}$]
400 nm
c
[20$\bar{2}$]
500 nm
d
[020]
APB tube
1 μm

Figure 7

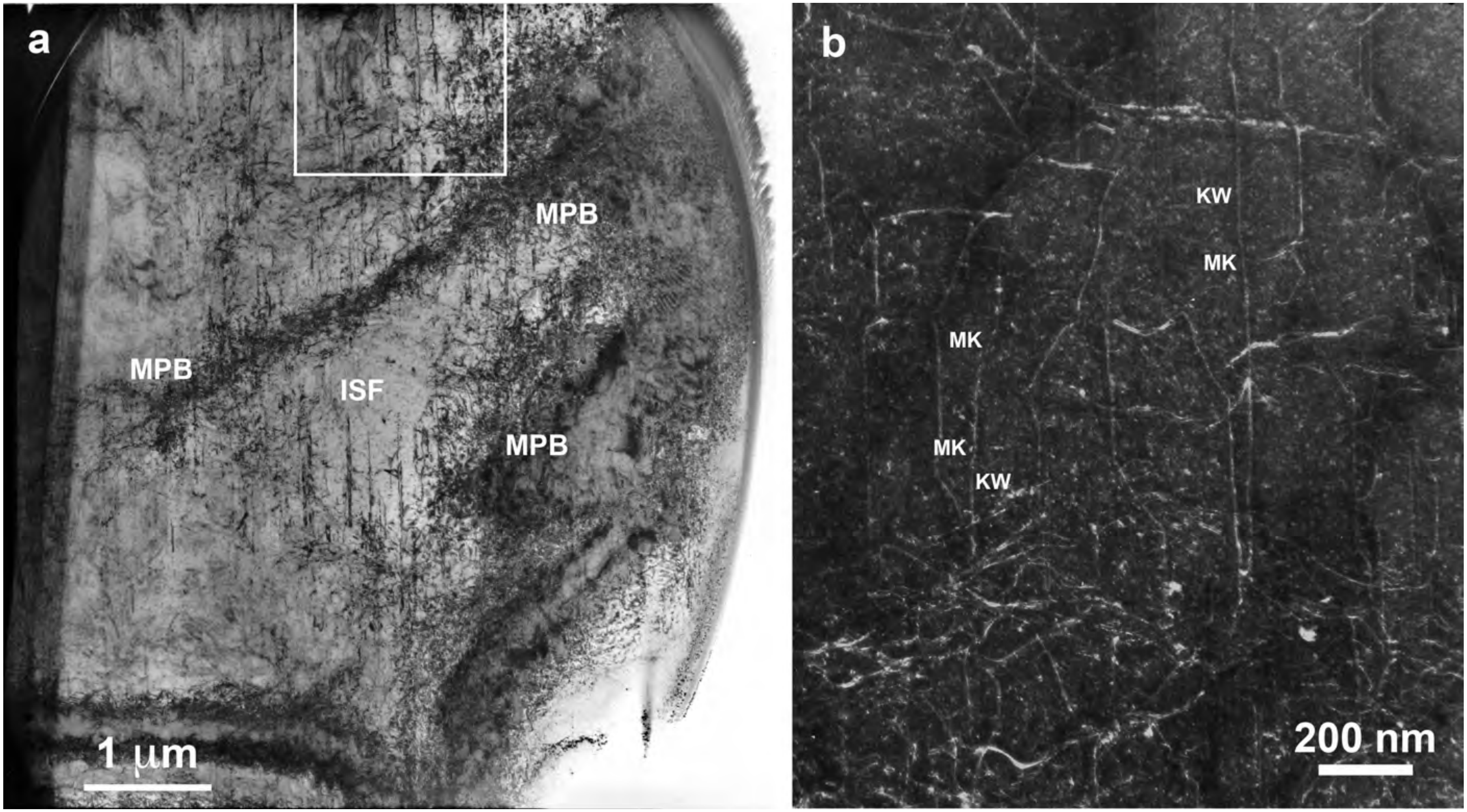
a
MPB
MPB
ISF
MPB
1 μm
b
KW
MK
MK
MK
KW
200 nm

Figure 8

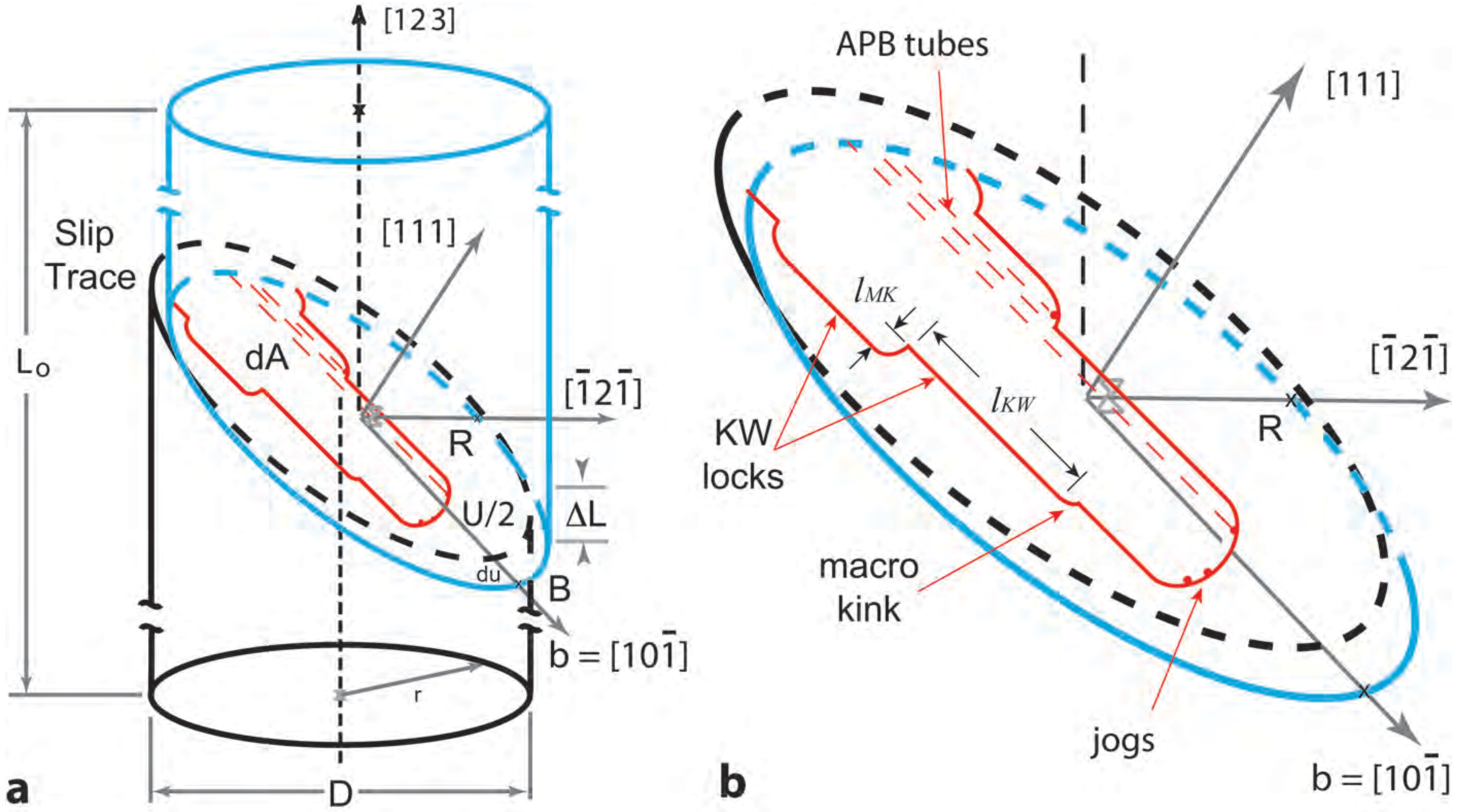

[123]
Slip Trace
[111]
L$_o$
dA
[$\bar{1}2\bar{1}$]
R
U/2
ΔL
du
B
b = [$10\bar{1}$]
r
a
D
APB tubes
[111]
l_{MK}
[$\bar{1}2\bar{1}$]
KW locks
l_{KW}
R
macro kink
jogs
b
b = [$10\bar{1}$]

Figure 9

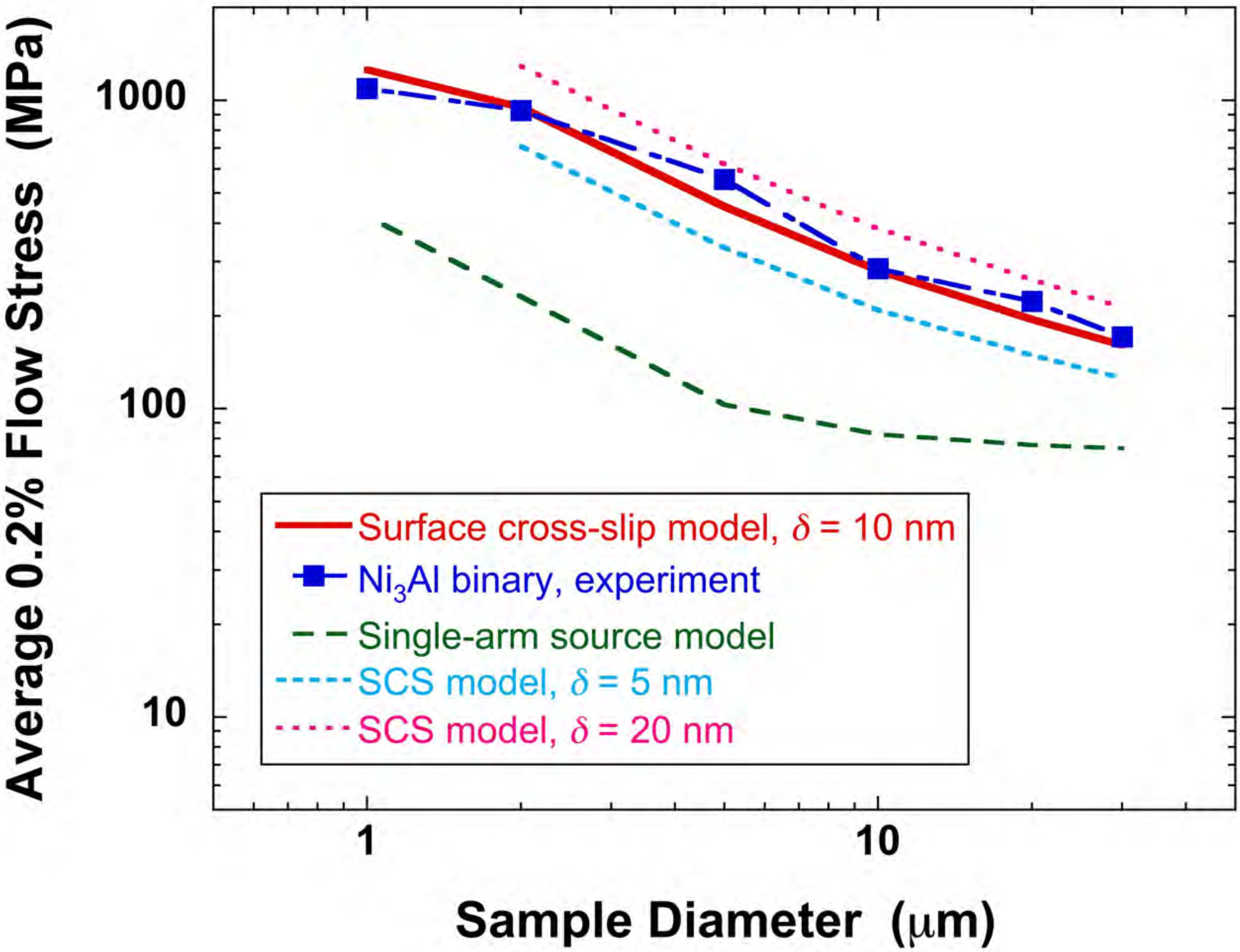
Average 0.2% Flow Stress (MPa)
1000
100
10
1
10
Sample Diameter (μm)
Surface cross-slip model, δ = 10 nm
Ni3Al binary, experiment
Single-arm source model
SCS model, δ = 5 nm
SCS model, δ = 20 nm

Figure 10

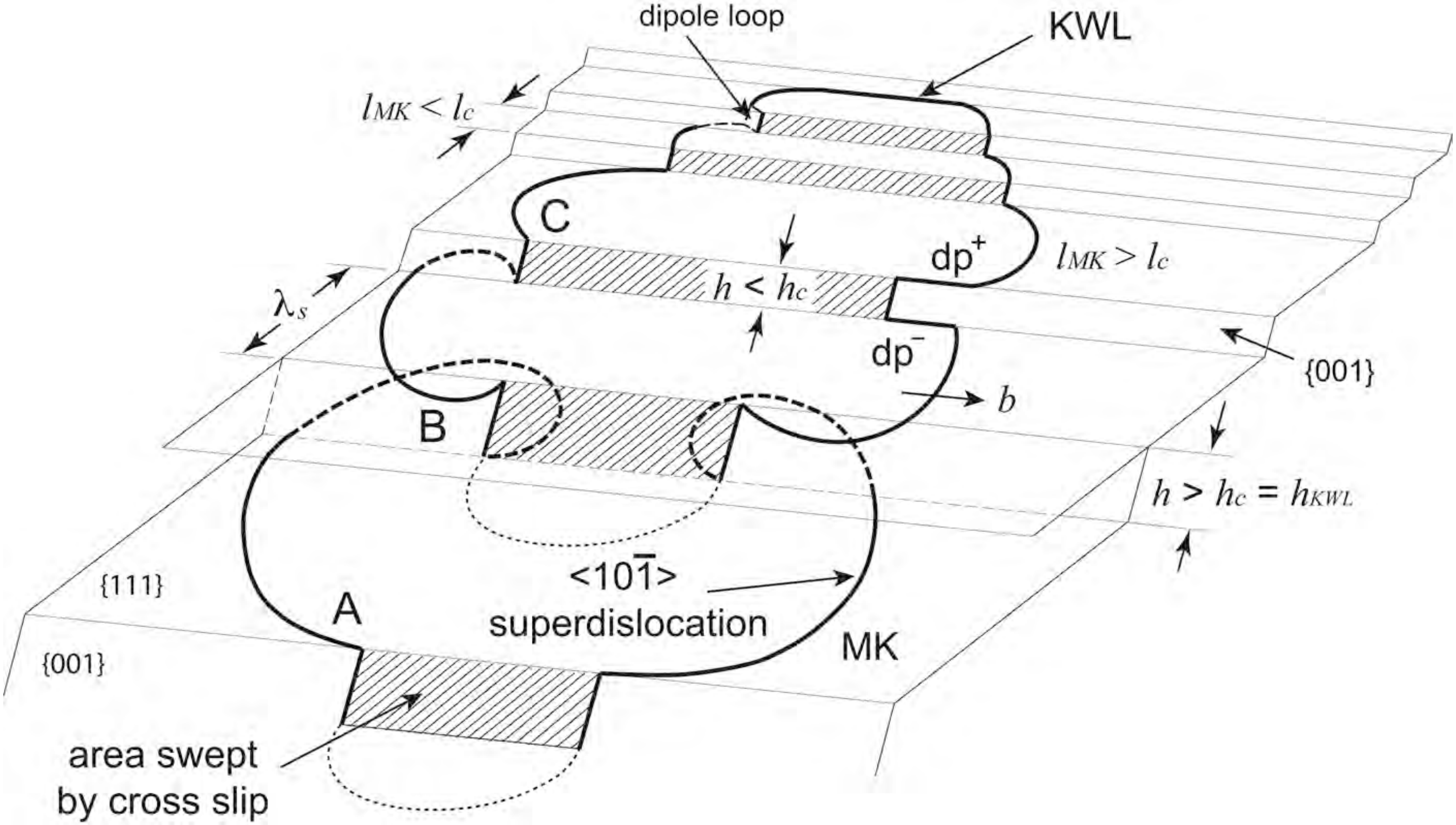

dipole loop
KWL
$l_{MK} < l_c$
C
dp^+
$l_{MK} > l_c$
λ_s
$h < h_c$
dp^-
{001}
B
b
$h > h_c = h_{KWL}$
{111}
<10$\bar{1}$>
A
superdislocation
MK
{001}
area swept
by cross slip

Figure 11

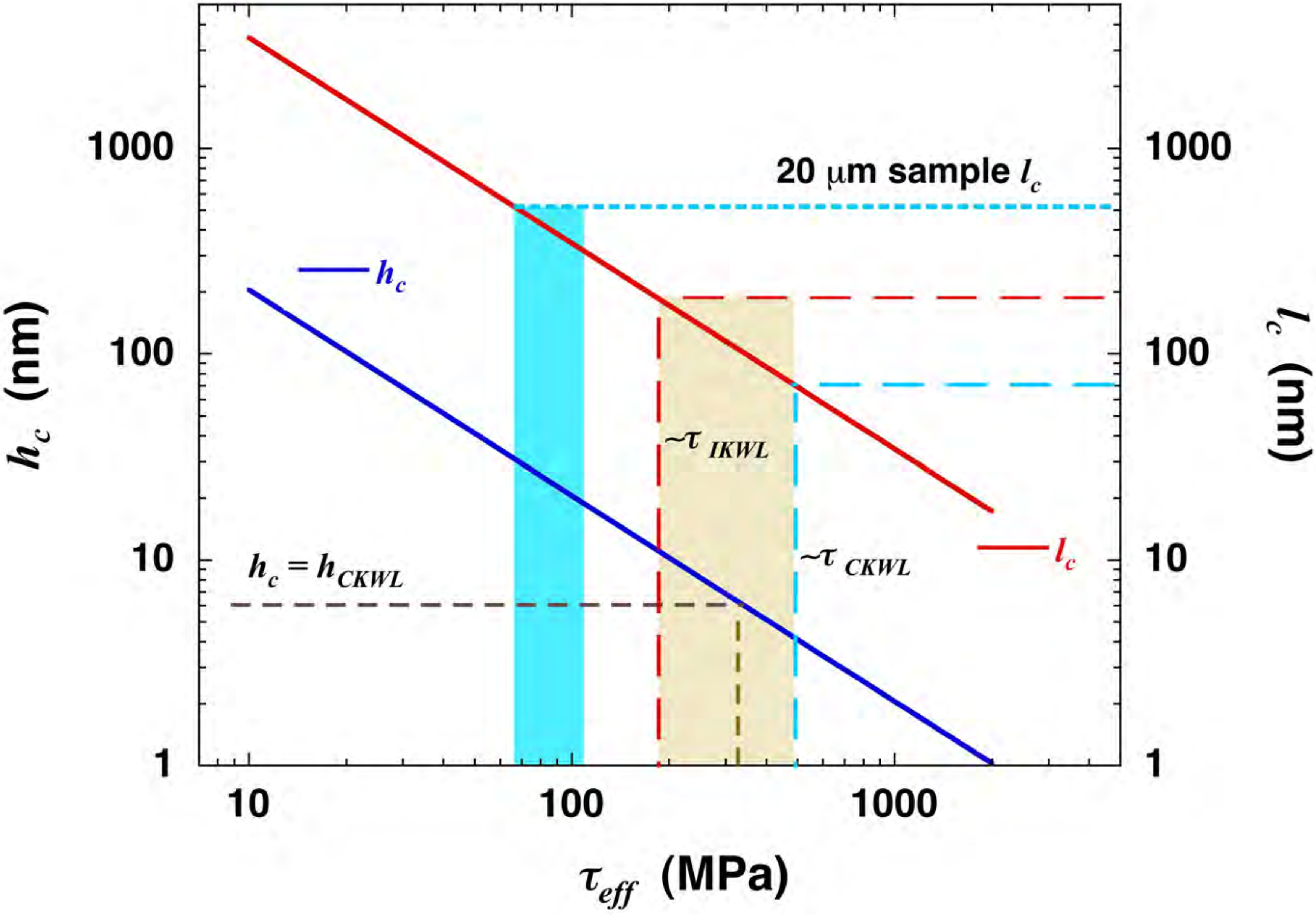
1000
100
10
1
10
100
1000
h_c (nm)
l_c (nm)
τ_{eff} (MPa)
20 μm sample l_c
h_c
l_c
$\sim\tau_{IKWL}$
$\sim\tau_{CKWL}$
$h_c = h_{CKWL}$

Figure 12

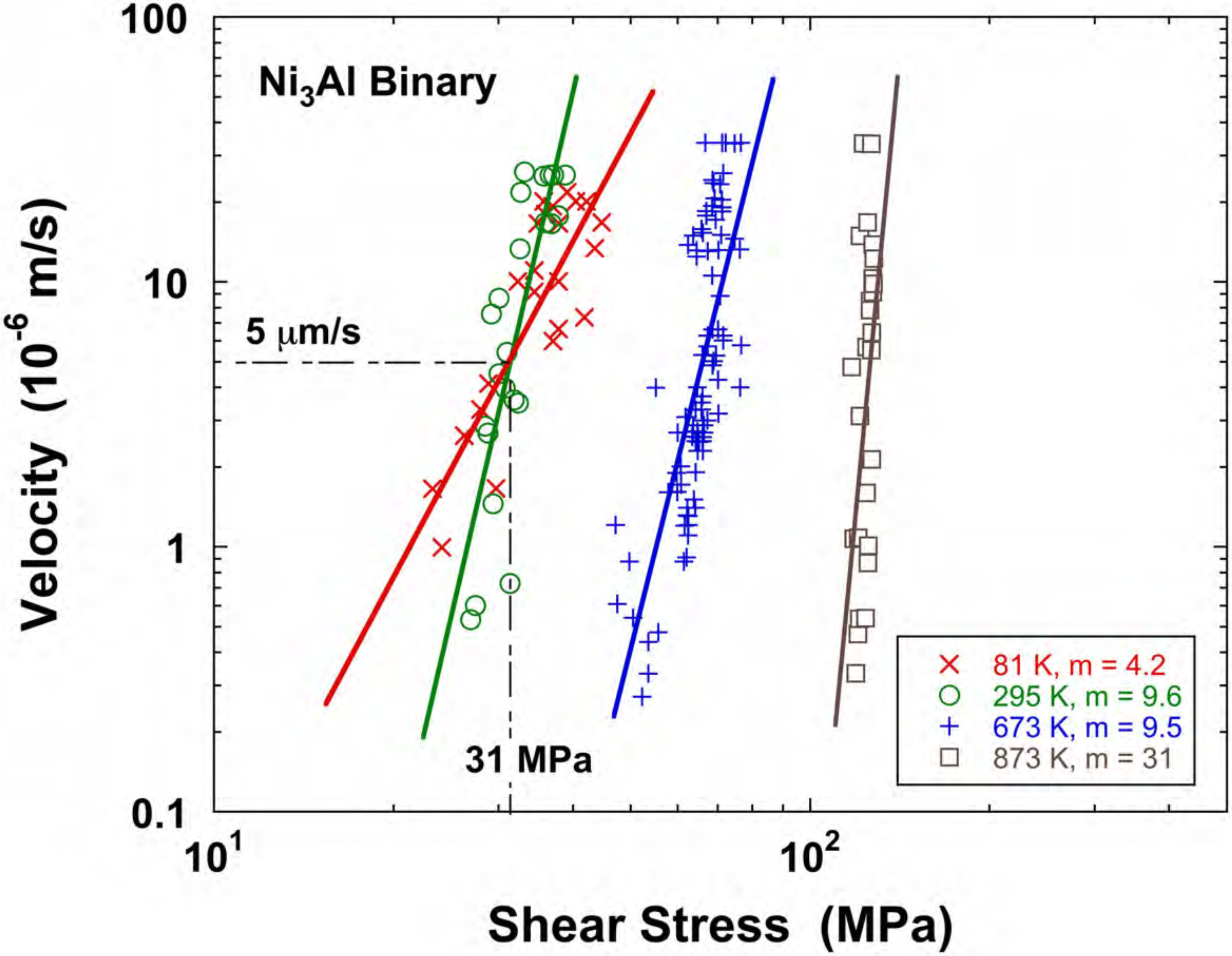
Ni3Al Binary
Velocity (10^-6 m/s)
100
10
1
0.1
5 μm/s
31 MPa
10^1
10^2
Shear Stress (MPa)
× 81 K, m = 4.2
○ 295 K, m = 9.6
+ 673 K, m = 9.5
□ 873 K, m = 31